JCB Journal of Cell Biology

ARTICLE

Sorting nexin 10 regulates lysosomal ionic homeostasis via ClC-7 by controlling PI(3,5)P_2

Jing Ze Wu[1,2], Joshua G. Pemberton[3,4], Shin Morioka[5,6], Junko Sasaki[5,6], Priya Bablani[1], Takehiko Sasaki[5,6], Tamas Balla[4], Sergio Grinstein[1,2], and Spencer A. Freeman[1,2]

Mutations or ablation of Snx10 are associated with neurodegeneration, blindness, and osteopetrosis. The similarities between osteoclasts and macrophages prompted us to analyze the role of Snx10 in phagocytosis. Deletion of Snx10 impaired phagosome resolution. Defective resolution was caused by reduced Cl^- accumulation within (phago)lysosomes, replicating the phenotype reported in macrophages lacking ClC-7, a lysosomal $2Cl^-/H^+$ antiporter. Delivery of ClC-7 to (phago)lysosomes was unaffected by ablation of Snx10, but its activity was markedly depressed. Snx10 was found to regulate ClC-7 activity indirectly by controlling the availability of phosphatidylinositol 3,5-bisphosphate (PI[3,5]P_2), which inhibits ClC-7. By limiting the formation of PI(3,5)P_2, Snx10 enables the accumulation of luminal Cl^- in phagosomes and lysosomes, which is required for their optimal degradative function. Our data suggest that Snx10 regulates the delivery of PI 3-phosphate (PI[3]P), the precursor of PI(3,5)P_2, from earlier endocytic compartments to (phago)lysosomes. By controlling the traffic of phosphoinositides, Snx10 regulates phagosomal resolution and possibly accounts for the impaired bone resorption in Snx10-deficient osteoclasts.

Introduction

Lysosomes are degradative compartments that effectively break down macromolecules taken up by endocytosis. They also serve to recycle components of effete organelles designated for autophagy (De Duve and Wattiaux, 1966; Perera and Zoncu, 2016; Pillay et al., 2002). In addition, lysosomes are also indispensable for immunity, digesting foreign particulate matter engulfed by phagocytosis, as well as supporting antigen processing and presentation (Delamarre et al., 2005; Honey and Rudensky, 2003; Styrt and Klempner, 1982). To these ends, the lysosomal lumen is replete with a vast array of hydrolytic enzymes. Their defective expression or activity leads to accumulation of incompletely degraded cargo, often causing lysosomal distention and disturbing cellular homeostasis (Chadwick et al., 2021b; Farfel-Becker et al., 2019; Platt et al., 2018; Xu and Ren, 2015). More recently, lysosomes have also been appreciated for participating in nutrient sensing and contributing to intracellular ionic homeostasis (Chadwick et al., 2021a; Mony et al., 2016; Rebsamen et al., 2015; Shin and Zoncu, 2020).

Critical to the maintenance of the degradative milieu inside lysosomes is the activity of the vacuolar-type ATPase (V-ATPase), which utilizes ATP to drive the influx of protons (H^+) into the organellar lumen (Ohkuma et al., 1982). The resulting luminal acidification (pH 4.5–5.0) not only provides an optimal environment for the activity of many of the hydrolases (Pillay et al., 2002), but the consequent establishment of a large H^+ gradient across the lysosomal membrane drives the coupled transport of a variety of organic and inorganic solutes. Co-transport with H^+ facilitates the export of amino acids (Löbel et al., 2022; Metzner et al., 2006), anionic sugars (Hu et al., 2023), and possibly dipeptides (Song et al., 2018), while counter-transport drives the accumulation of inorganic ions (Melchionda et al., 2016; Wartosch et al., 2009). The exchange of cytosolic chloride anions (Cl^-) for intralysosomal H^+ best illustrates the latter modality. ClC-7, an integral protein of the lysosomal-limiting membrane, has been convincingly established to catalyze the uptake of two Cl^- in exchange for a single H^+, a notably rheogenic process (Leisle et al., 2011; Wartosch et al., 2009; Wu et al., 2023; Zhang et al., 2020). By virtue of the large transmembrane H^+ gradient, ClC-7 drives the accumulation of Cl^- in the lysosomal lumen, where the concentration of the anion markedly exceeds the cytosolic concentration. Of note, the elevated luminal [Cl^-] was previously shown to be essential to establish an optimal degradative milieu inside lysosomes (Wartosch et al., 2009; Zhang et al., 2023) and phagolysosomes (Wu et al., 2023). The inherent chloride dependence of several degradative enzymes is thought to account,

[1]Program in Cell Biology, Hospital for Sick Children, Toronto, Canada; [2]Department of Biochemistry, University of Toronto, Toronto, Canada; [3]Department of Biology, Faculty of Science, Western University, London, Canada; [4]Section on Molecular Signal Transduction, Eunice Kennedy Shriver National Institute of Child Health and Human Development, National Institutes of Health, Bethesda, MD, USA; [5]Department of Biochemical Pathophysiology, Medical Research Institute, Tokyo Medical and Dental University, Tokyo, Japan; [6]Department of Lipid Biology, Graduate School of Medical and Dental Sciences, Tokyo Medical and Dental University, Tokyo, Japan.

Correspondence to Sergio Grinstein: sergio.grinstein@sickkids.ca; Spencer A. Freeman: spencer.freeman@sickkids.ca.

at least in part, for these observations (Aghajari et al., 2002; Cigic and Pain, 1999).

Loss-of-function mutations in ClC-7 have been characterized and linked to several diseases (e.g., neurodegeneration and osteopetrosis) (Kasper et al., 2005; Kornak et al., 2001; Majumdar et al., 2011). The neurodegeneration and accompanying susceptibility to blindness have been attributed to the impaired ability of phagocytic cells, including microglia and macrophages, to clear extracellular debris, while the osteopetrosis is due to defective bone resorption by osteoclasts, which are developmentally and functionally related to phagocytes. Interestingly, osteopetrosis is also caused by mutation (Pangrazio et al., 2013; Stattin et al., 2017) or deletion (Ye et al., 2015; Zhou et al., 2016) of Snx10, a small phosphoinositide-binding protein implicated in membrane traffic (Barnea-Zohar et al., 2021). Mutations in Snx10 are also associated with presentations of blindness and neurological symptoms (Pangrazio et al., 2013; Stattin et al., 2017). Moreover, a CRISPR screen revealed that, similar to ClC-7 and its chaperone, OSTM1, Snx10 confers sensitivity to apilimod, a selective inhibitor of PIKfyve, the enzyme responsible for phosphatidylinositol (PI) 3,5-bisphosphate (PI[3,5]P_2) biosynthesis (Gayle et al., 2017). These similarities prompted us to study if, like ClC-7, Snx10 plays a role in (phago)lysosomal function and whether its effects are attributable to changes in Cl^- transport and degradative capacity.

Results

Snx10 is required to maintain the degradative capacity of phagosomes and lysosomes

While mutations in Snx10 were reported to lead to the development of disease (Aker et al., 2012; Pangrazio et al., 2013; Stattin et al., 2017), the underlying molecular mechanisms remain obscure. To better understand its mode of action, we initially edited *Snx10* to generate Snx10 knockouts (KO) in RAW 264.7 macrophages, a phagocytic cell line. The effective deletion of Snx10 was validated by immunoblotting: as illustrated in Fig. 1 A, the protein was undetectable in two separate KO lines, which were selected for further study. To compare the degradative capacity of these cells, WT and Snx10 KO macrophages were challenged with IgG-opsonized sheep RBCs (sRBCs), which were taken up and contained within phagosomes. The extent of target degradation after 1 and 4 h was assessed by monitoring the sRBC volume, as described previously (Wu et al., 2023). In stark contrast to WT macrophages, which degraded the internalized sRBC almost entirely over 4 h, Snx10 KO macrophages were unable to break down the targets over the same time period (Fig. 1, B and C).

The failure of Snx10-deficient cells to degrade internalized sRBC could be attributable to a loss of hydrolytic activity within phagolysosomes, as reported for ClC-7 KO macrophages (Wu et al., 2023). To test this possibility, WT and Snx10 KO macrophages were challenged with IgG-opsonized silica beads that were coated with dye-quenched BSA (DQ-BSA), an indicator of proteolytic activity. Cleavage of DQ-BSA by proteases delivered to the phagosome through fusion with lysosomes results in an increase in the fluorescence signal. As illustrated in Fig. 1 D and quantified in Fig. 1 E, the proteolytic effectiveness of phagolysosomes was reduced by ≈50% in cells lacking Snx10, which resembles the phenotype of ClC-7 KO cells (Wu et al., 2023).

Most (phago)lysosomal proteases, including those of the cathepsin family, are synthesized as catalytically inactive precursors (zymogens) that only become active following an (auto) proteolytic cleavage transition (Muno et al., 1993). To determine whether Snx10 is important for the proteolytic maturation of cathepsins, lysates of WT and Snx10 KO macrophages were probed with anti-cathepsin C antibody. Snx10 KO cells displayed elevated levels of unprocessed, immature cathepsin C (~55 kDa) and reduced levels of the mature cathepsin C band (~25 kDa), compared with the parental WT cells (Fig. 1, F and G). Thus, defective conversion of the zymogens to their active counterparts contributes to the reduced proteolytic activity of Snx10-deficient phagolysosomes.

Phagosome maturation and acidification are independent of Snx10

The defective resolution of the contents of phagosomes in Snx10-deficient macrophages may be caused by improper (incomplete) maturation (i.e., failure to merge with lysosomes) or by their inability to fully acidify their lumen; the latter mechanism is compatible with the reported association of Snx10 with the D subunit of the V-ATPase (Chen et al., 2012), which could conceivably be required for optimal H^+ pumping. These possibilities were examined in turn. The rate and extent of phagosome maturation were assessed by visualizing the acquisition of LAMP1, a widely used marker of late (endo)lysosomes. As anticipated, nascent phagosomes (formed by WT cells within 3 min of adding the targets) were largely devoid of LAMP1; after maturing for 30 min, the phagosomes became richly endowed with this marker (Fig. 2 A). Importantly, Snx10 KO macrophages behaved similarly (Fig. 2 A), implying that delayed or incomplete maturation to phagolysosomes was not responsible for their failure to degrade the engulfed targets. This conclusion was further supported by ratiometric determinations of the phagosomal pH. Consistent with earlier findings, the luminal pH of phagosomes formed following ingestion of sRBC labeled with FITC—a pH-sensitive fluorophore—was highly acidic (pH ≤ 5.0) and was indistinguishable between WT and Snx10 KO macrophages (Fig. 2 B). A profound acidification was also observed when phagosomes contained FITC-labeled opsonized zymosan particles and was identical in WT and Snx10 KO cells (Fig. 2 C). In both instances the luminal acidification was dissipated by addition of concanamycin A (CCA), a specific inhibitor of the V-ATPase. Therefore, we concluded that its reported interaction with Snx10 is not essential for proton pumping by the (phago) lysosomal V-ATPase.

Snx10 is required for the accumulation of Cl^- in (phago) lysosomes

Phagosomes and lysosomes contain high luminal [Cl^-], which was recently shown to directly support the activity of resident hydrolases, fostering the degradation of phagosomal targets (Wu et al., 2023; Zhang et al., 2023). Importantly, the accumulation of Cl^- in these organelles is driven by ClC-7 or its homologue, and

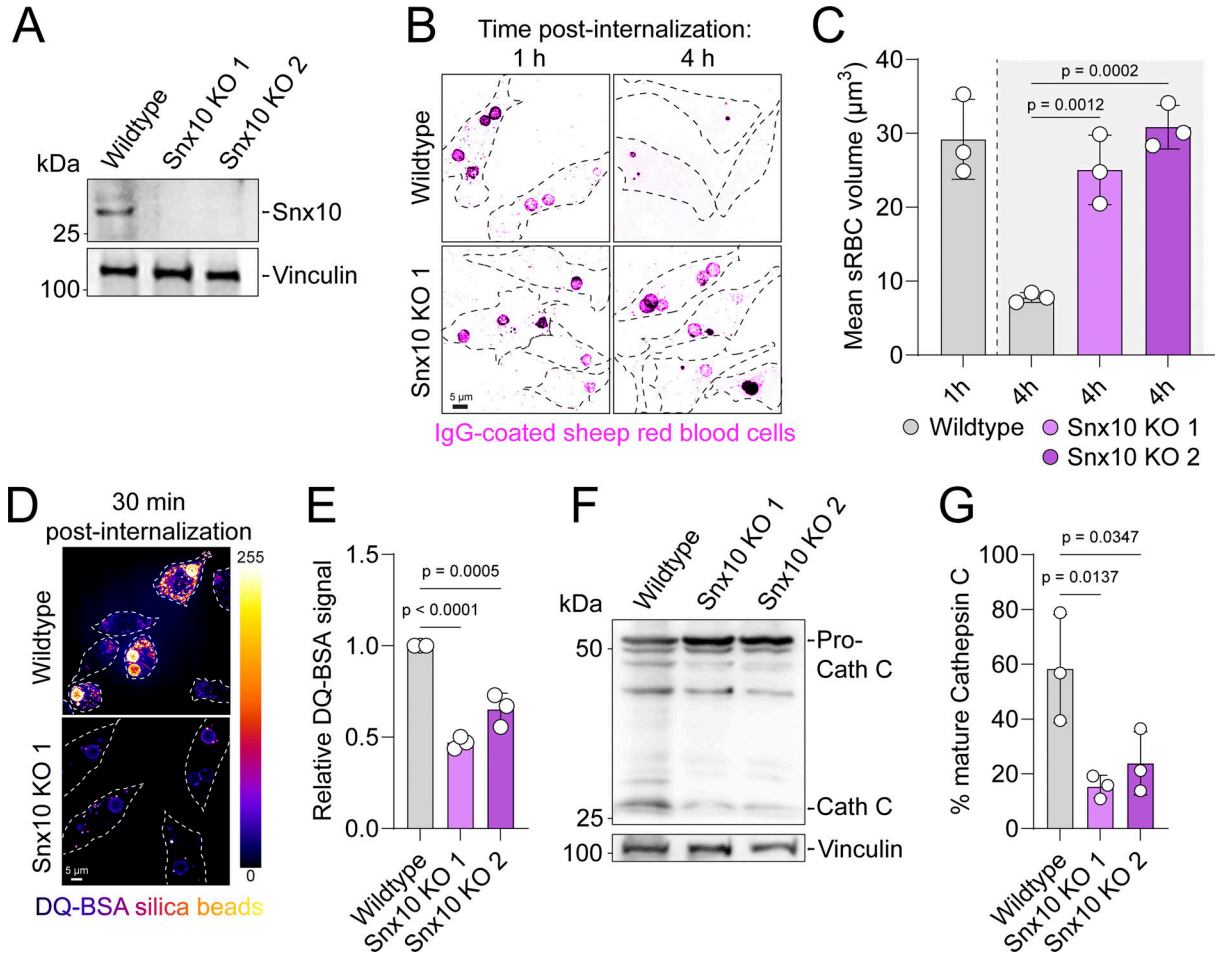

Figure 1. **Snx10 is required for proper degradative capacity of phagosomes and lysosomes. (A)** Lysates of WT and two separate Snx10 KO RAW 264.7 cell clones were probed with anti-Snx10 and anti-vinculin antibodies (used to normalize loading) and analyzed by SDS-PAGE. Molecular weight markers (kDa) are indicated. **(B and C)** WT and Snx10 KO RAW 264.7 cells challenged with IgG-coated sRBCs and visualized 1 or 4 h after phagocytosis with anti-IgG antibody (magenta). Images in B are representative of three independent experiments. Mean ± SD of sRBC phagosome volumes were quantified at 1 and 4 h in C. *n* = 3 independent experiments, each counting >70 phagosomes. **(D)** Representative fluorescence images of WT and Snx10 KO RAW 264.7 cells challenged with IgG- and DQ-BSA–coated silica beads for 30 min. DQ-BSA signal is presented in pseudocolor. **(E)** Quantification of relative DQ-BSA fluorescence intensity in WT and Snx10 KO RAW 264.7 cells. *n* = 3, each independent experiment measuring >25 phagosomes. **(F)** Lysates of WT and Snx10 KO cells probed with anti-cathepsin C (Cath C) antibody and anti-vinculin antibody used to normalize loading. The position of pro-cathepsin and mature (cleaved) cathepsin are indicated. Molecular weight markers (kDa) indicated on left. **(G)** Quantification of mature cathepsin C levels relative to the total cathepsin C. *n* = 3.

deletion of this antiporter impaired phagosomal resolution without affecting phagosome maturation or acidification (Wu et al., 2023), closely resembling the phenotype of Snx10-deficient cells. We therefore considered the possibility that Snx10 deletion might impair Cl^- accumulation in (phago)lysosomes. Two separate approaches were used to estimate the Cl^- concentration in lysosome-related organelles in WT and Snx10 KO macrophages. The first method involves the colorimetric determination of chloride in cell extracts using mercury thiocyanate and ferric nitrate. Two strategies were applied to maximize the contribution of lysosomes in collected cell extracts to the Cl^- determinations: first, the lysosomal volume was greatly increased by overnight incubation with sucrose (Fig. 3 A), which accumulates in the lysosomal lumen as it cannot be hydrolyzed or transported across the limiting membrane (Bright et al., 2016; Cai et al., 2024). As a result, the enlarged lysosomes (sucrosomes) occupy a sizeable fraction of the total cellular volume, which becomes readily apparent when trapping fluorescent dextrans within their lumen (Fig. 3 B). Note that, as is the case for intact lysosomes, ClC-7 is distinctly present in the sucrosomal-limiting membrane (Fig. S1 A). Moreover, sucrosomes display robust proteolytic activity that is markedly depressed when ClC-7 or Snx10 are deleted (Fig. S1 B), indicating that they are suitable mimics of lysosomes. To further increase the contribution of lysosomes/sucrosomes to the Cl^- determinations, the cytosolic Cl^- was leached from the cells by permeabilizing the plasma membrane briefly (30 s) while bathing the cells in Cl^--depleted (gluconate-substituted) medium; this was accomplished by activating plasmalemmal P_2X_7 receptors with ATP (Fig. 3 A). The effectiveness of the permeabilization step was verified using FM1–43, a small (m.w. 611) solvochromic dye that stains only the outer leaflet of the plasma membrane of intact cells, but readily enters ATP-permeabilized cells, staining endomembranes (Fig. 3 C). The integrity of the enlarged

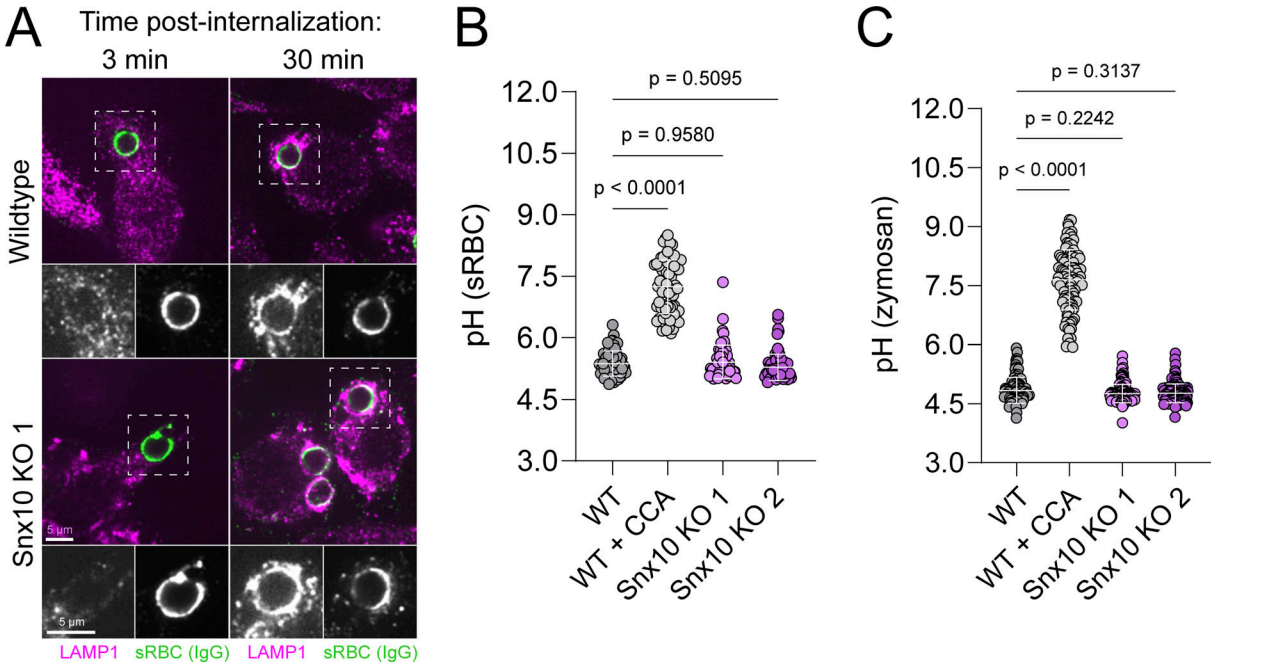

Figure 2. **Phagosomal maturation and acidification occur independently of Snx10. (A)** WT and Snx10 KO RAW 264.7 cells challenged with IgG-opsonized sRBCs for 3 or 30 min, then immunostained with anti-LAMP1 antibodies and visualized with fluorescent secondary antibodies against the antibodies opsonizing the sRBCs (green) and the anti-LAMP1 antibodies (magenta). **(B and C)** WT and Snx10 KO RAW 264.7 cells were challenged with IgG-opsonized, FITC-conjugated sRBCs (B), or zymosan particles (C) for 1 h prior to imaging. The steady-state pH of >100 phagosomes from three independent experiments is shown. Where noted, 500 nM of concanamycin A (CCA) was used for 30 min prior to imaging to neutralize phagosomal pH.

lysosomal membrane is preserved under the gentle permeabilization conditions used, as indicated by the persistence of the transmembrane H^+ gradient, detected by the accumulation of cresyl violet (Ostrowski et al., 2016). Using this approach and considering the total sucrosomal volume determined by integrating the fluorescence of the trapped dextran, the sucrosomal [Cl^-] was determined to be 129.7 + 2.9 mM in WT cells (Fig. 3 D), which agrees with previous measurements of (phago) lysosomal [Cl^-] (Riazanski et al., 2021; Tan et al., 2013; Wu et al., 2023). Sucrosomal accumulation of Cl^- occurs in exchange for luminal H^+, a process mediated by ClC-7. This is indicated by the reduced [Cl^-] detected following treatment with CCA, as well as in sucrosomes formed in ClC-7 KO cells. Strikingly, sucrosomal Cl^- was also greatly reduced in Snx10 KO cells (Fig. 3 D).

To validate the results obtained in sucrosomes, we also estimated [Cl^-] in normal lysosomes loaded with 10,10′-bis[3-carboxypropyl]-9,9′-biacridinium dinitrate (BAC)—a fluorophore that is quenched by high [Cl^-] (Sonawane et al., 2002)—which had been covalently conjugated to 10 kDa amino dextran to ensure its retention within lysosomes. To account for the varying size and shape of lysosomes, the fluorescence of BAC was normalized to that of AlexaFluor-647–labeled dextran and, because precise calibration of BAC inside lysosomes is difficult and unreliable, the results are presented relative to untreated, WT lysosomes. In agreement with the sucrosome data, we found the relative lysosomal [Cl^-] to be markedly reduced following the inhibition of the V-ATPase and also in the absence of ClC-7, compared with the untreated WT (Fig. 3 E). More importantly, lysosomal [Cl^-] was also depressed in the two Snx10 KO clones, confirming that Snx10 is required for the accumulation of lysosomal Cl^-, presumably by enabling the activity of ClC-7.

Snx10 does not affect the delivery of ClC-7 to (phago) lysosomes

The preceding results suggest that Snx10 controls the uptake of Cl^- into lysosomes by modulating ClC-7 activity. Because sorting nexins have been implicated in membrane traffic, we considered the possibility that Snx10 may be required to deliver ClC-7 to lysosomes and phagolysosomes. To this end, WT, ClC-7 KO, and Snx10 KO macrophages were challenged with IgG-opsonized targets (silica beads) and, after 1 h, were fixed, permeabilized and immunostained with anti–ClC-7 antibody. As expected, ClC-7 was clearly detectable in the limiting membrane of WT phagosomes but not in those formed by ClC-7 KO macrophages (Fig. 4, A and B), attesting to the specificity of the antibodies used. Phagosomes formed by Snx10 KO macrophages displayed ClC-7 levels comparable with those of WT phagosomes (Fig. 4, A and B), indicating that the sorting nexin is not required for targeting the antiporter to (phago)lysosomes. To determine whether endolysosomal morphodynamics were more broadly altered upon loss of Snx10, WT, ClC-7 KO, and Snx10 KO macrophage lysosomes were visualized by pulse labeling with 10 kDa tetramethylrhodamine dextran overnight. Loss of Snx10 had no discernible effect on the tubulovesicular morphology of lysosomes in RAW 264.7 cells (Fig. S1 C). Nevertheless, endolysosomal maturation dynamics could conceivably be affected by the loss of Snx10. To assess this, we first labeled the lysosomes of WT and Snx10 KO macrophages with an overnight pulse chase of

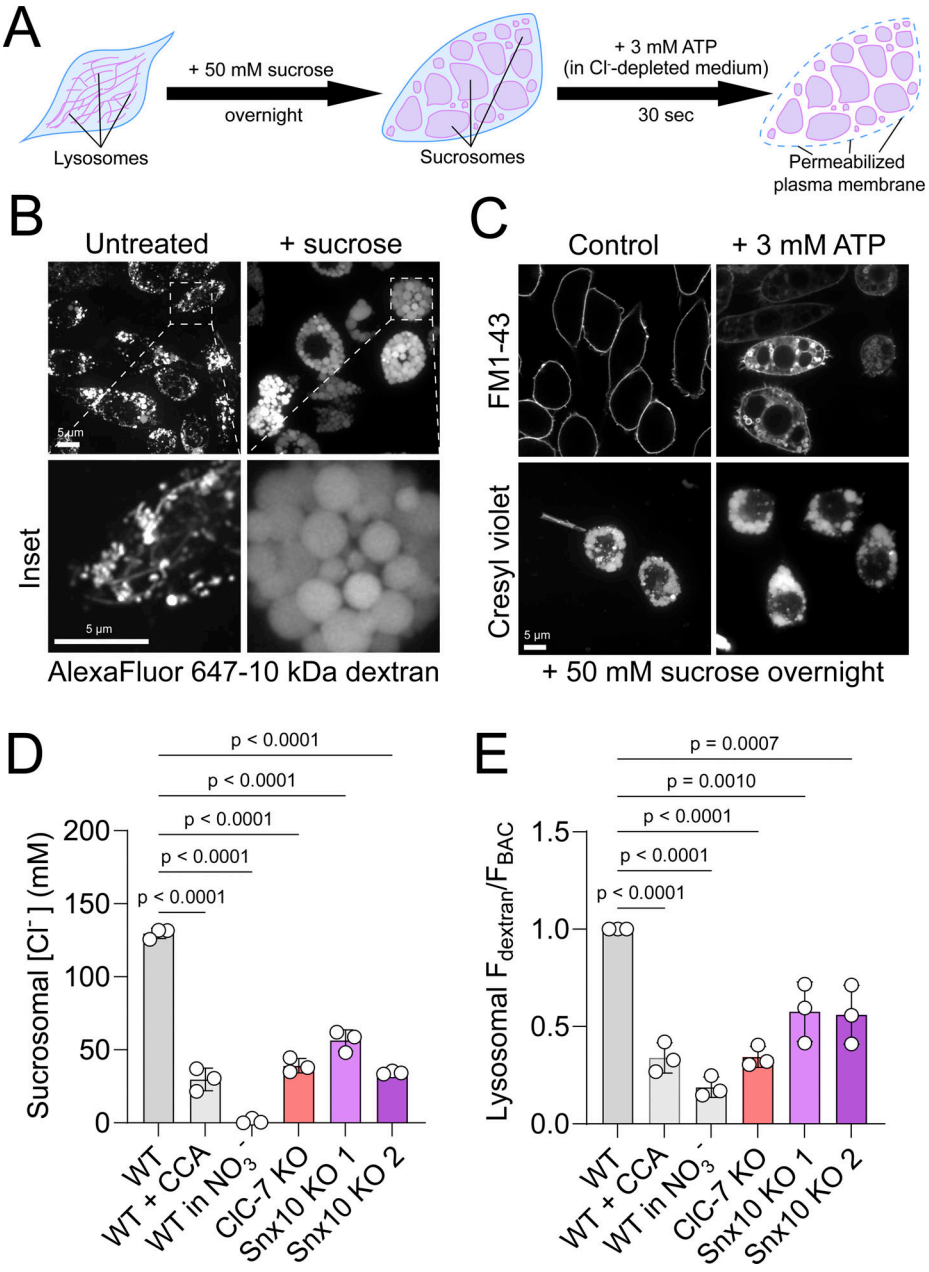

Figure 3. **Snx10 supports the accumulation of high luminal [Cl^-] within endolysosomes. (A)** Schematic of procedure used for [Cl^-] determinations in sucrosomes. RAW 264.7 macrophages were incubated overnight (16 h) in medium containing 50 mM sucrose, then acutely treated with 3 mM ATP for 30 s in sodium gluconate medium (devoid of Cl^-) to permeabilize the plasma membrane via the engagement of purinergic receptors, thereby rapidly depleting cytosolic [Cl^-]. **(B)** Representative fluorescence images of sucrosome formation in RAW 264.7 macrophages. Cells were pulsed with AlexaFluor-647–conjugated 10 kDa dextran overnight in medium with or without added sucrose, then chased with fresh medium for 1 h prior to imaging. Insets represent times times (3×) zoom images of indicated regions of interest. **(C)** Cells incubated in the presence of 50 mM sucrose overnight were treated with either vehicle control or 3 mM ATP for 30 s in Na-gluconate medium, then labeled with either FM1–43 dye (top) or cresyl violet (bottom) prior to imaging. **(D)** Sucrosomal [Cl^-] was determined colorimetrically as detailed in Materials and methods in WT, CCA-treated (WT + CCA), Cl^--substituted for nitrate (WT in NO_3^-), ClC-7 KO, and Snx10 KO cells prepared as described in A. n = 3. **(E)** Relative lysosomal [Cl^-] was determined in WT, CCA-treated (WT + CCA), Cl^--substituted for nitrate (WT in NO_3^-), ClC-7 KO, and Snx10 KO cells using BAC-conjugated 10 kDa dextran as described in Materials and methods. n = 3.

10 kDa tetramethylrhodamine dextran, followed by an acute incubation with 10 kDa AlexaFluor-647 dextran for 10–30 min to observe bulk fluid uptake and transit along the endocytic pathway. Loss of Snx10 had no noticeable effect on the transit kinetics of fluid phase markers from early to late endocytic compartments (Fig. S1 D).

Snx10 regulates ClC-7 activity by controlling the level of PI(3,5)P_2

Because the targeting of ClC-7 to (phago)lysosomes appeared to be unaffected by Snx10, we instead considered that the transport activity of the antiporter may be regulated by the sorting nexin, whether directly or indirectly. It was previously reported that

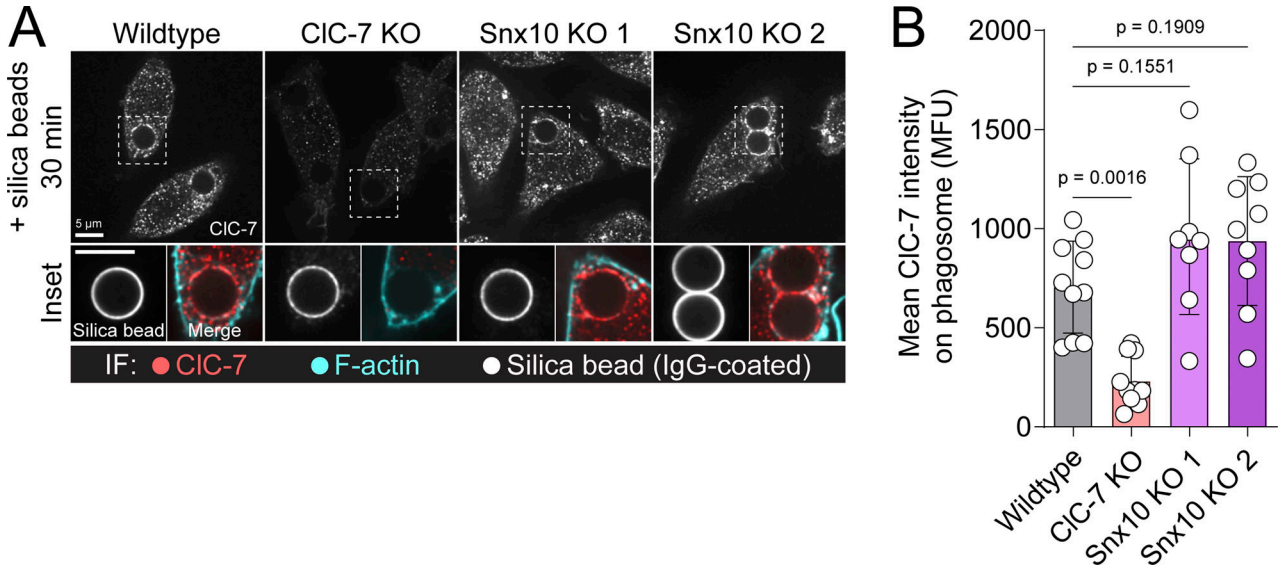

Figure 4. **Delivery of ClC-7 to mature phagosomes does not require Snx10. (A)** WT, ClC-7 KO, and Snx10 KO RAW 264.7 macrophages were challenged with IgG-opsonized silica beads for 30 min prior to fixing. Cells were then stained with anti-ClC-7 antibodies (red), phalloidin (Acti-Stain 488; cyan), and anti-IgG antibodies (white in insets). **(B)** Mean ClC-7 signal intensity on phagosomes, measured in three independent experiments. MFU = mean fluorescence units.

ClC-7 and its *Arabidopsis* homologue ClC-a are strongly inhibited by PI(3,5)P_2, a rare signaling phosphoinositide (Carpaneto et al., 2017; Leray et al., 2022). Importantly, PI(3,5)P_2 has been detected in late endocytic compartments (Takatori et al., 2016), where ClC-7 is known to reside. Given that Snx10 has been demonstrated to bind the precursor of PI(3,5)P_2, PI 3-phosphate (PI[3]P) (Barnea-Zohar et al., 2021; Yao et al., 2009) (Fig. S1 E), which it requires for both its vesicular localization (Fig. S1 F) and vacuolating effect upon overexpression (Fig. S1 G), we inquired whether the expression of the sorting nexin influences the levels of these phosphoinositides. To distinguish PI(3,5)P_2 from its more abundant bisphosphorylated regioisomers (e.g., PI[4,5]P_2 and PI[3,4]P_2), we employed a combination of chiral column chromatography and triple-stage quadrupole tandem mass spectrometry (see Morioka et al. [2022] for details). This analysis revealed a greater than twofold increase in the PI(3,5)P_2 content of Snx10 KO cells, compared with their WT counterparts (Fig. 5 A). The increase was evident in multiple replicates of the two Snx10 KO clones. A more modest, yet significant increase in PI(3)P content was also detected in the Snx10 KO cells (Fig. 5 B). By contrast, all other phosphoinositides, including PI(4,5)P_2 and PI(3,4,5)P_3, as well as other common phospholipid species analyzed (phosphatidylcholine [PC], phosphatidylethanolamine [PE], phosphatidylserine [PS], phosphatidylglycerol [PG], and phosphatidic acid [PA]), were all found at similar levels in WT and Snx10 KO macrophages (Fig. S2, A–I), confirming that equivalent quantities of cells were analyzed in all instances.

The above findings suggest that Snx10 influences the activity of ClC-7 by controlling the availability of PI(3,5)P_2. This model predicts that pharmacologically ablating PI(3,5)P_2 should preclude the effect of Snx10 KO on the activity of the antiporter. This prediction was tested experimentally by comparing the sucrosomal [Cl^-] of WT and Snx10 KO macrophages that had been incubated in the presence of YM201636, a potent PIKfyve inhibitor (Jefferies et al., 2008). Contrary to untreated sucrosomes, where the [Cl^-] of WT cells is markedly higher than that of Snx10 KO cells (see Fig. 3 D and also Fig. 5 C), sucrosomes of cells that were treated with YM201636 for 30 min showed no significant differences; [Cl^-] was elevated regardless of the deletion of Snx10 (Fig. 5 C).

Based on the finding that PI(3,5)P_2 depresses the activity of ClC-7 (Leray et al., 2022) and ClC-a (Carpaneto et al., 2017), we predicted that inhibition of PIKfyve would unleash Cl^- transport across the lysosomal membrane via the antiporter. Accordingly, and in good agreement with previous observations (Gayle et al., 2017; Ikonomov et al., 2001; Jefferies et al., 2008; Kim et al., 2014), pharmacological ablation of PI(3,5)P_2 caused the overactivation of ClC-7 that manifested as a profound swelling of the late endolysosomal (ClC-7-positive; Fig. S3 A) compartments, which was readily visualized by preloading with fluorescent fluid-phase markers (Fig. 5, D and E; Fig. S1 C; and Fig. S5 H). In sharp contrast, endolysosomal swelling resulting from PIKfyve inhibition failed to occur in ClC-7–deficient cells, supporting the notion that the antiporter mediates the volume gain induced by inhibition of PIKfyve (Fig. 5, D and E; and Fig. S1 C). Importantly, swelling persisted in the absence of Snx10 (Fig. 5, D and E; and Fig. S1 C), implying that the sorting nexin exerts its effect on ClC-7 by modifying PI(3,5)P_2.

The enlargement of the (endo)lysosomes induced by pharmacological inhibition of PIKfyve enabled us to measure their Cl^- content colorimetrically, as described for Fig. 3, but without having to resort to sucrose preloading (Fig. S3 B). As documented in Fig. S3 C, the swelling caused by ablation of PI(3,5)P_2 was accompanied by lysosomal accumulation of Cl^-, which occurred independently of Snx10.

Lysosomal swelling was also recently reported to occur in patient fibroblasts expressing hyperactive variants of ClC-7 (ClC-7^{Y715C} or ClC-7^{K285T}) that cause a novel type of lysosomal

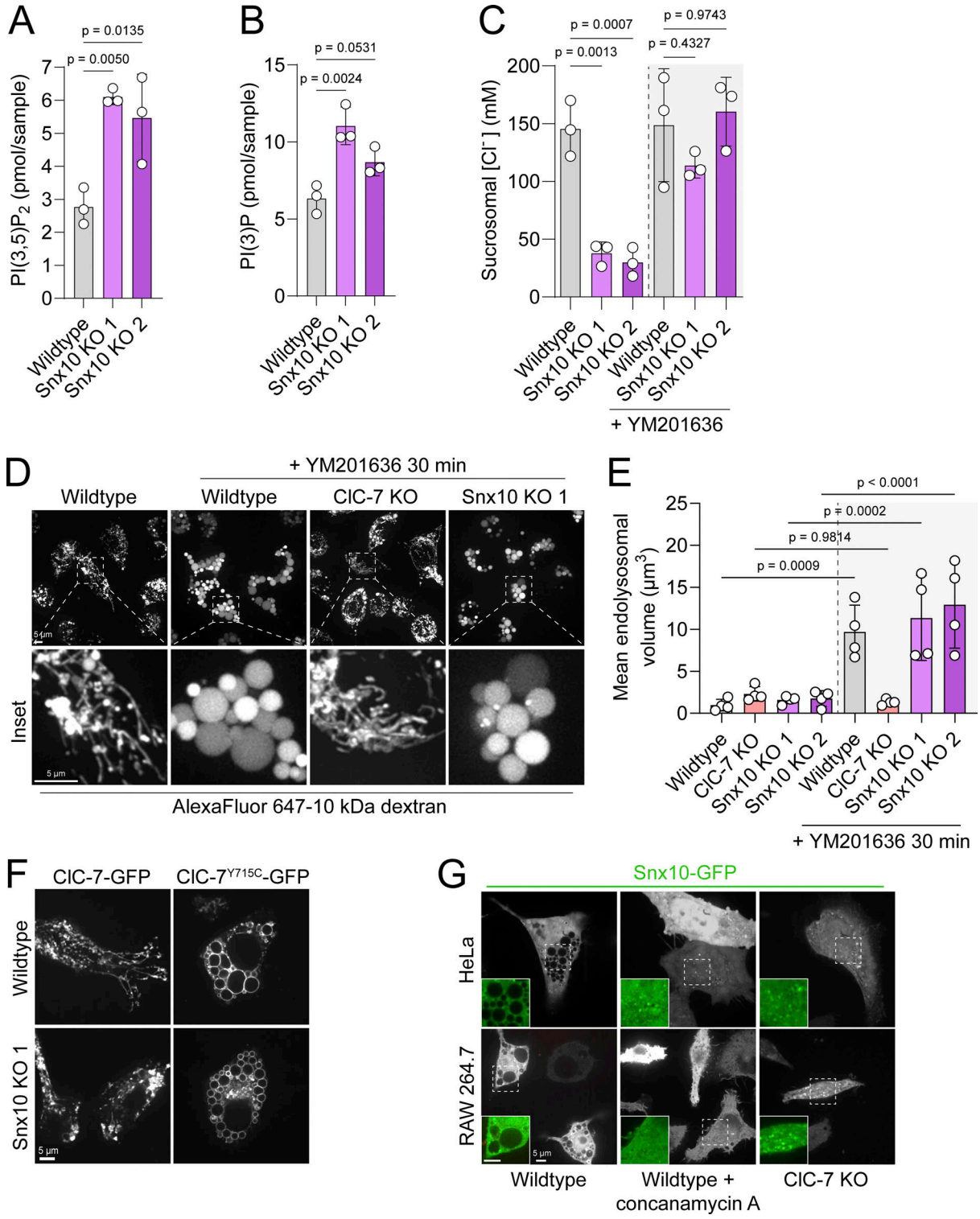

Figure 5. **Snx10 dictates ClC-7 activity by modulating cellular PI(3,5)P_2 levels. (A and B)** Phosphoinositide levels in WT and Snx10 KO RAW 264.7 macrophages determined by PRMC-MS: (A) PI(3,5)P_2; (B) PI(3)P. **(C)** Sucrosomal [Cl^-] of WT and Snx10 KO RAW 264.7 macrophages treated with vehicle control or 100 nM YM201636 for 30 min [Cl^-] was determined colorimetrically as outlined in Fig. 3 A; *n* = 3. **(D)** Representative fluorescence images of lysosomes in WT, ClC-7 KO, and Snx10 KO RAW 264.7 macrophages. Lysosomes were visualized by pulsing overnight with AlexaFluor-647–conjugated 10 kDa dextran and chasing for 1 h prior to imaging. Where indicated, the cells were treated with either 100 nM YM201636 or vehicle as control for 30 min immediately prior to imaging. Lower row shows five times (5×) zoom images of regions denoted by dashed lines. **(E)** Mean vacuole volumes determined from images like those in D and Fig. S1 C. *n* = 3. **(F)** WT and Snx10 KO RAW 264.7 macrophages were transiently transfected with either ClC-7-GFP or ClC-7^{Y715C}-GFP for 18 h prior to imaging GFP. **(G)** WT and ClC-7 KO HeLa (top 3 panels) and RAW 264.7 (bottom 3 panels) cells were imaged 16 h after being transiently transfected with Snx10-GFP (green). Where indicated, the cells were treated with either 500 nM CCA or vehicle only for 1 h prior to imaging. Images are representative of three independent experiments. PRMC-MS: phosphoinositide regioisomer measurement by chiral column chromatography and mass spectrometry.

storage disorder (Nicoli et al., 2019; Polovitskaya et al., 2024). Interestingly, the excessive activity conferred by these mutations in ClC-7 is associated with—and seemingly attributable to—desensitization of the exchanger to $PI(3,5)P_2$ (Leray et al., 2022); as such, expression of these variants affords a convenient model to probe the mode of action of Snx10. As shown in Fig. 5 F, the swelling phenotype described in fibroblasts expressing ClC-7^{Y715C} could be readily replicated when this variant was heterologously expressed in RAW 264.7 macrophages. Revealingly, the lysosomal swelling induced by expression of ClC-7^{Y715C} persisted in cells lacking Snx10, consistent with the notion that the sorting nexin alters the availability of phosphoinositides, rather than targeting the H^+/Cl^- antiporter directly. Treatment with YM201636, a PIKfyve inhibitor, did not further enlarge the swollen compartments of WT and Snx10 KO macrophages expressing ClC-7^{Y715C}, suggesting that these compartments were maximally swollen (Fig. S3 D).

The elevated $PI(3,5)P_2$ and depressed ClC-7 activity detected in Snx10-deficient cells suggest that Snx10 limits the generation and/or delivery of $PI(3,5)P_2$ to lysosomes. According to this model, overabundance of Snx10 is anticipated to have the opposite effect, namely activation of ClC-7 resulting from reduced $PI(3,5)P_2$ in lysosomes. This prediction was tested through the heterologous overexpression of Snx10. Transient transfection (overexpression) of Snx10-GFP led to profound endomembrane swelling in both RAW 264.7 macrophages and HeLa cells (Fig. 5 G). The swollen compartment was both Rab7- and ClC-7-positive (Fig. S3, E and F), indicative of its lysosomal identity. Moreover, the swelling caused by Snx10 overexpression required the presence of ClC-7 and was precluded by inhibition of the V-ATPase (Fig. 5 G). Jointly, these observations indicate that overexpression of Snx10 results in hyperactivation of ClC-7.

Snx10 controls the availability of $PI(3,5)P_2$ on ClC-7-positive organelles

We interpreted the preceding results to mean that the overexpression of Snx10 stimulated ClC-7 activity by reducing the availability of $PI(3,5)P_2$ in the lysosomal compartment, where the antiporter resides. Because there are currently no reliable means to quantify subcellular $PI(3,5)P_2$—specifically in lysosomes—we instead tested our hypothesis by attempting to reverse the stimulation of ClC-7 induced by Snx10 overexpression by forcibly repleting $PI(3,5)P_2$ in lysosomes. This was accomplished using a newly developed approach by which an engineered and highly active catalytic fragment of PIKfyve (catalytic core; CC) is selectively recruited to an organelle of choice, where, if the requisite PI(3)P substrate is present, $PI(3,5)P_2$ is generated de novo (Pemberton et al., 2025). Targeted recruitment was accomplished using rapamycin-induced heterodimerization. As illustrated in Fig. 6 A, the kinase fusion protein (mRFP-FKBP-PIKfyve^{CC}) can be rapidly recruited to late (endo)lysosomes endowed with Rab7 using the iRFP-FRB-Rab7 targeting construct, causing accumulation of $PI(3,5)P_2$ in this compartment. The localized production of $PI(3,5)P_2$ was demonstrated in live cells using an optimized variant of a recently described $PI(3,5)P_2$-specific biosensor (Vines et al., 2023) termed NES-mNG-NES-(2x)*Dd*SnxA^{PX} (Pemberton et al., 2025), which, while failing to reveal any steady-state enrichment of $PI(3,5)P_2$ in subcellular membranes, effectively detects the excess phosphoinositide generated upon recruitment of the engineered kinase construct to the PI(3)P-containing endosomal compartments.

The heterodimerization system enabled us to test whether ectopic generation of $PI(3,5)P_2$ on Rab7-positive compartments could revert the swelling phenotype induced by Snx10 overexpression. Strikingly, the large vacuoles formed by cells overexpressing Snx10 began shrinking shortly after $PI(3,5)P_2$ was synthesized by the recruited kinase, virtually disappearing within an hour (Fig. 6, B and D). Importantly, the vacuoles persisted throughout this period when an inactive form of the kinase (mRFP-FKBP-PIKfyve^{CC} K1877A) was recruited (Fig. 6, C and D), indicating that neither the transfection procedure nor the addition of rapamycin were themselves responsible for the vacuolar shrinkage, which must instead be attributed to the de novo formation of $PI(3,5)P_2$.

While these data corroborated the notion that Snx10 modulates ClC-7 activity by controlling the level of $PI(3,5)P_2$ in lysosomes, it remained unclear how Snx10 could function to impact the levels of the phosphoinositide. Interestingly, Snx10 has been reported to physically interact with PIKfyve (Bao et al., 2021), raising the possibility that it could directly inactivate the kinase. Alternatively, Snx10 might delay the delivery of PI(3)P to lysosomes or activate/recruit a phosphatase(s) that can reduce the levels of either PI(3)P or $PI(3,5)P_2$. These possibilities were analyzed by taking advantage of the heterodimerization-induced recruitment of the active FKBP-PIKfyve^{CC} fragment. As shown in Fig. 6 A, recruitment of the kinase to Rab7-containing membranes rapidly increased their $PI(3,5)P_2$ content, as revealed by the NES-mNG-NES-(2x)*Dd*SnxA^{PX} biosensor. Importantly, the increase in $PI(3,5)P_2$ was more pronounced in the Snx10 KO cells than in their WT counterparts, despite comparable levels of recruitment of the active kinase (Fig. 6 E; and Fig. S4, A and B). This was not the case when the kinase was recruited to Rab5-containing vesicles (Fig. 6 F; and Fig. S4, C and D), implying that Snx10 selectively affects phosphoinositide metabolism in Rab7-positive, late (endo)lysosomal compartments. The greater accumulation of $PI(3,5)P_2$ in the Rab7-positive compartments of Snx10-deficient cells (Fig. 6 E; and Fig. S4, A and B) implies that the sorting nexin either promotes clearance of the phosphoinositide or delays the delivery of PI(3)P, the substrate of PIKfyve, from upstream compartments.

The latter explanation is consistent with the observations reported in Fig. 6, G and H (illustrated in Fig. S4, E and F), where the presence of PI(3)P was assessed using a probe (Kanai et al., 2001) based on the PX domain of $p40_{phox}$ ($p40_{phox}^{PX}$). A small but significant fraction of the Rab7-containing vesicles were decorated by the $p40_{phox}^{PX}$ probe, indicative of the presence of PI(3)P in late (endo)lysosomal compartments. Compared with WT macrophages, the fraction of $p40_{phox}^{PX}$- and Rab7-positive (endo)lysosomes was considerably greater in both Snx10 KO clones (Fig. 6 G and Fig. S4 E), while the fraction of $p40_{phox}^{PX}$- and Rab5-positive (endo)lysosomes was modestly decreased (Fig. S5, A and B). Conversely, fewer late (endo)lysosomes recruited $p40_{phox}^{PX}$ in HeLa cells, where Snx10 had been heterologously overexpressed, although the difference did not reach statistical significance (Fig. 6 H and Fig. S4 F). The fraction of

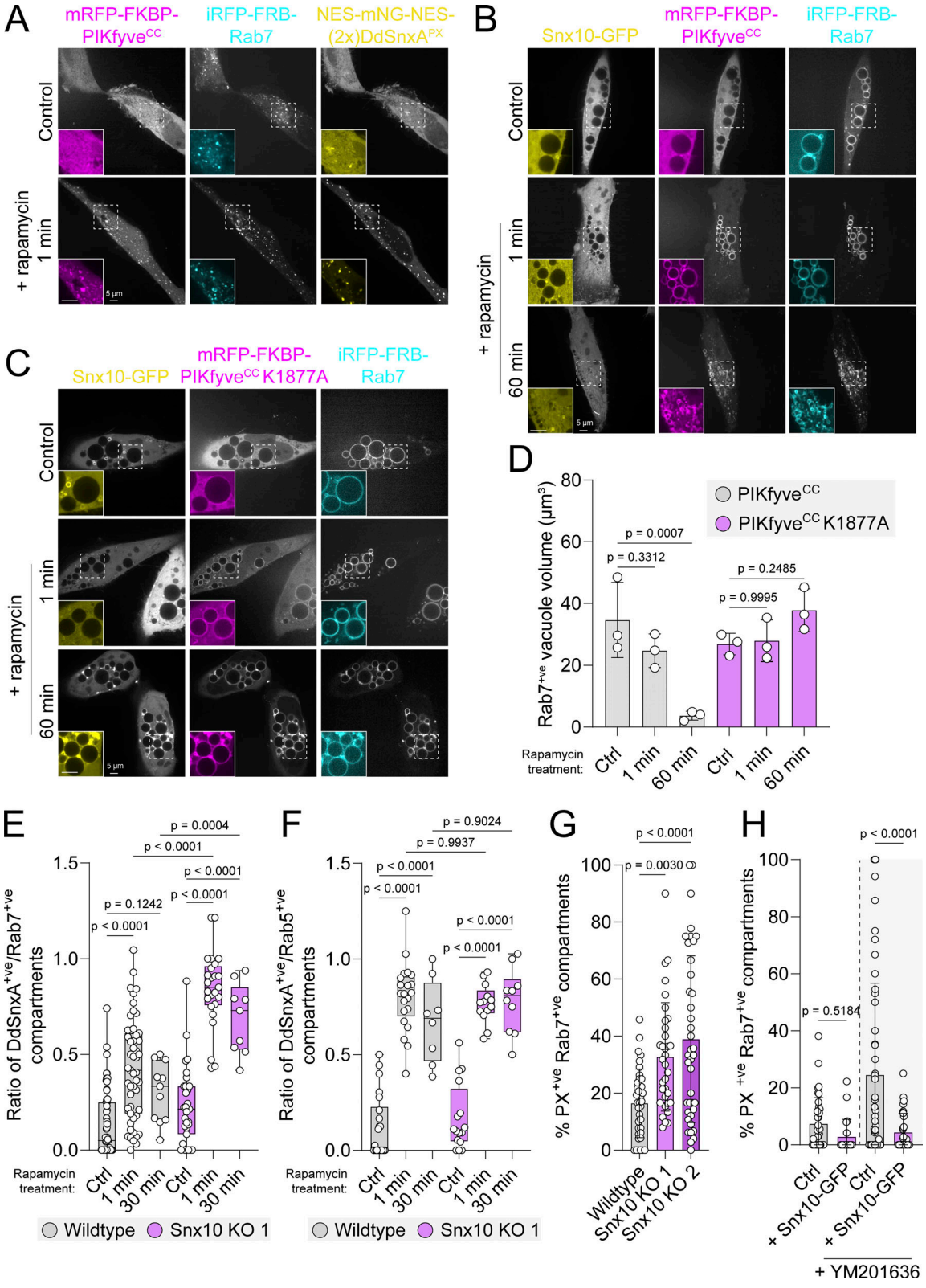

Figure 6. **Snx10 controls levels of PI(3,5)P_2 on late endolysosomes. (A)** HeLa cells were transiently transfected with mRFP-FKBP-PIKfyve^{CC}, iRFP-FRB-Rab7, and NES-mNG-NES-(2x)*Dd*SnxA^{PX} 18 h prior to imaging. Representative fluorescence images of cells prior to (top 3 panels) and 1 min after the addition of 100 nM rapamycin (bottom 3 panels). **(B and C)** HeLa cells transiently transfected with Snx10-GFP, iRFP-FRB-Rab7, and either (B) mRFP-FKBP-PIKfyve^{CC} or (C) mRFP-FKBP-PIKfyve^{CC} K1877A for 18 h prior to imaging. Representative fluorescence images of cells before (top 3 panels), 1 min (middle 3 panels) or 60 min after the addition of 100 nM rapamycin (bottom 3 panels). **(D)** Mean volume of Rab7-positive vacuoles from experiments like those represented in B and C. *n* = 3, each point representing the average volume of >30 vacuoles. **(E and F)** WT (grey) and Snx10 KO RAW 264.7 cells (magenta) were transiently transfected with

NES-mNG-NES-(2x)*Dd*SnxA^{PX}, mRFP-FKBP-PIKfyve^{CC}, and either (E) iRFP-FRB-Rab7 or (F) iRFP-FRB-Rab5 for 12 h prior to imaging. The ratio of NES-mNG-NES-(2x)*Dd*SnxA^{PX}–positive compartments to either (E) iRFP-FRB-Rab7 or (F) iRFP-FRB-Rab5 before 1 min and 30 min after addition of 100 nM rapamycin is shown. *n* = 3. **(G)** WT and Snx10 KO RAW 264.7 macrophages were co-transfected with PX-GFP and mRFP-Rab7. The percentage of organelles found to be positive for both markers is indicated. *n* = 3. **(H)** HeLa cells were co-transfected with both p40$_{phox}^{PX}$-RFP and iRFP-FRB-Rab7 (control), and Snx10-GFP where indicated, then subject to treatment with either vehicle control or 100 nM YM201636 for 30 min prior to imaging. The percentage of organelles found to be positive for both p40$_{phox}^{PX}$ and Rab7 is indicated. *n* = 3.

late (endo)lysosomes labeled with p40$_{phox}^{PX}$ increased markedly when PIKfyve was inhibited by YM201636 and, under these circumstances, the effect of Snx10 became more noticeable and statistically significant (Fig. 6 H and Fig. S4 F). It is important to note that under these conditions, there was no observed overlap between Rab5 and Rab7 compartments, ruling out the possibility that PIKfyve inhibition increased PI(3)P on Rab7 compartments via the formation of hybrid compartments (Fig. S5 G). To determine whether this difference in PI(3)P localization along the endocytic pathway had an effect on the distribution of PI(3)P-binding proteins, we compared the localization of early endosome antigen 1 (EEA1), a known PI(3)P effector, in WT and Snx10 KO cells. We found that loss of SNX10 had no appreciable effect on the localization of EEA1 to early Rab5-positive vesicles but did led to a slight increase in the percentage of Rab7-positive compartments that associated with EEA1 (Fig. S5, C–F), which agrees with the observations made in Fig. 6 G and Fig. S4 E. Jointly, these data favor the notion that Snx10 restricts the delivery of PI(3)P to late (endo)lysosomes and hence its conversion to PI(3,5)P_2 by PIKfyve. Deletion of the sorting nexin enhances the availability and levels of the substrate (PI(3)P) (Fig. 5 B) and, as a consequence, also the enzymatic product of PIKfyve, PI(3,5)P_2, which ultimately restrains the activity of ClC-7.

The degradative capacity of phagosomes is dictated by the control of ClC-7 activity by PI(3,5)P_2

Given the regulatory relationship between Snx10 and ClC-7, the defects in phagosome resolution observed in Snx10 KO macrophages may be ascribed to altered regulation of the antiporter by PI(3,5)P_2. If this were the case, uncoupling the activity of ClC-7 from its regulation by the phosphoinositide would be anticipated to overcome the effects of deleting Snx10. This prediction was tested by heterologously expressing the PI(3,5)P_2-insensitive variant ClC-7^{Y715C} in Snx10 KO macrophages. These cells were then challenged with sRBC, and their ability to degrade the phagocytic cargo was monitored. While as reported in Fig. 1, A and B, Snx10-deficient macrophages failed to break down their phagocytic cargo; expression of the phosphoinositide-insensitive form of ClC-7 restored their ability to degrade sRBC over 4 h, as illustrated in Fig. 7, A and B. Thus, Snx10 acts to control the activity of ClC-7 in cells by restricting the abundance of PI(3,5)P_2 on mature (phago)lysosomes.

Discussion

We report that macrophages lacking Snx10 fail to degrade their engulfed cargo contained within phagolysosomes. In principle, this impaired degradation could result from an inability of Snx10-deficient phagosomes to acidify their lumen; accordingly, inhibition of the V-ATPase responsible for (phago)lysosomal acidification has been repeatedly demonstrated to inhibit cargo degradation (Lo and Zeng, 2023; Lukacs et al., 1990; Moriwaki et al., 2024; Wu et al., 2023; Zhang et al., 2022). This possibility is lent credence by the reported physical interaction between Snx10 and the V-ATPase (Chen et al., 2012). However, our measurements indicate that the pH of Snx10-deficient phagolysosomes is highly acidic, indistinguishable from that of WT cells (Fig. 2, B and C), thereby ruling out impaired acidification as the mechanism underlying defective phagolysosome resolution.

Instead, our results indicate that altered [Cl^-] homeostasis is responsible for the inability of Snx10 KO macrophages to degrade their cargo (Fig. 3). Cl^- is required for the optimal activity of multiple lysosomal hydrolases (Aghajari et al., 2002; Cigic and Pain, 1999; Wu et al., 2023), and failure to accumulate this anion was earlier shown to account for the defective degradation of lysosomal and (phago)lysosomal content in ClC-7 KO cells (Wu et al., 2023; Zhang et al., 2023). Furthermore, we find that target degradation can be rescued in Snx10 KO macrophages by expression of a constitutively active variant of ClC-7. Jointly, these observations indicate that the effect of Snx10 is exerted through regulation of the activity of ClC-7.

Abnormal delivery of ClC-7 could in theory explain the inability of Snx10 KO phagolysosomes to accumulate Cl^-. However, direct visualization and quantitation of (phago)lysosomal ClC-7 content (Fig. 4, A and B) compelled us to dismiss this possibility. Rather, our data indicate that Snx10 affects the regulation of ClC-7 through spatial changes to membrane phosphoinositide composition. Specifically, deletion of Snx10 causes accumulation of PI(3,5)P_2 in (phago)lysosomes, which in turn depresses the activity of the antiporter. Several conceivable mechanisms could account for the observed alteration in PI(3,5)P_2 levels. First, the sorting nexin, which has been shown to associate with PIKfyve (Bao et al., 2021), could directly inhibit its lipid kinase activity. Multiple lines of evidence argue against this mechanism. First, the catalytic domain of PIKfyve (mRFP-FKBP-PIKfyve^{CC}) increased PI(3,5)P_2 to a greater extent when recruited to the Rab7 compartment in Snx10 KO than in WT cells, yet phosphoinositide accumulation was comparable when recruited to the Rab5 compartment, where most of the Snx10 resides. Secondly, deletion of Snx10 was associated with increased total PI(3)P (Fig. 5 B) and with increased recruitment of the p40$_{phox}^{PX}$ probe to Rab7 compartments (Fig. 6 G and Fig. S4 E), while the opposite would be expected had the activity of PIKfyve been increased. This contrasts with observations made when expressing a hyperactive mutant of PIKfyve, in which case a drop in PI(3)P accompanied the overproduction of PI(3,5)P_2 (McCartney et al., 2014). Together, these data suggest that direct

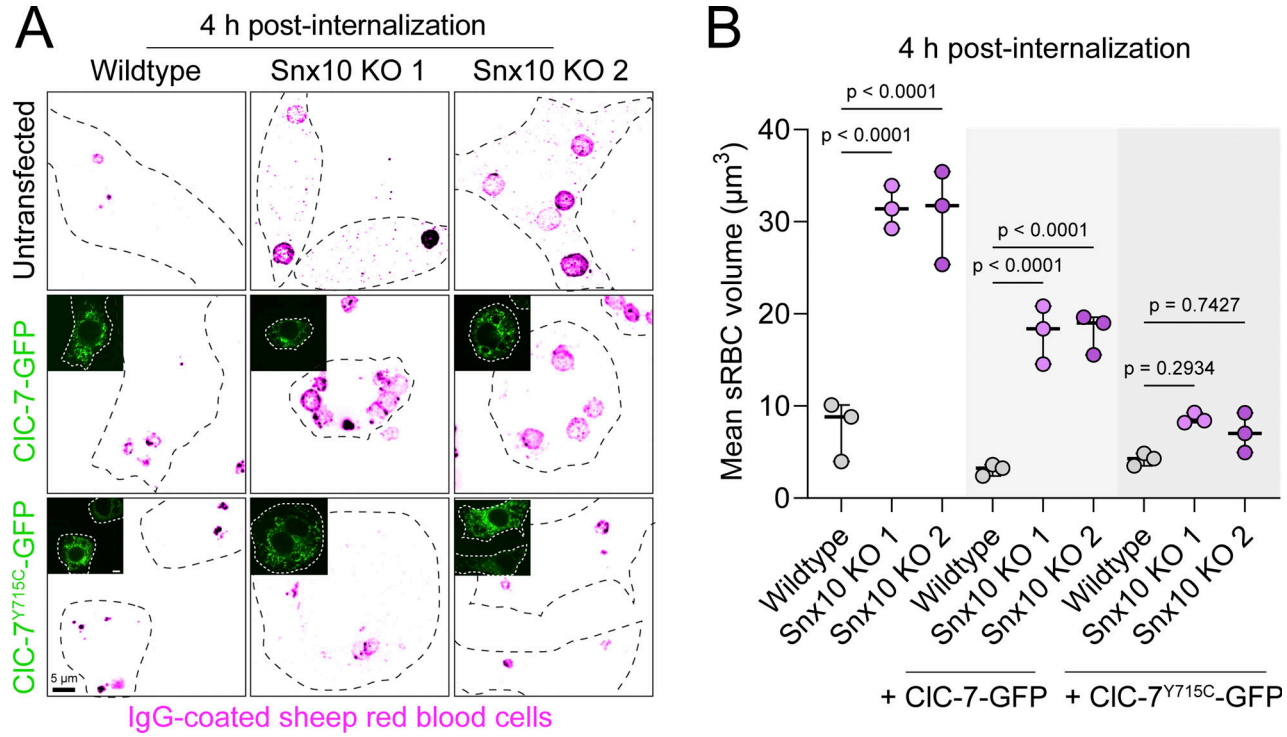

Figure 7. **Phagosomal resolution is driven by sensitivity of ClC-7 to PI(3,5)P_2. (A)** WT and Snx10 KO RAW 264.7 macrophages were either untransfected (top row) or transiently transfected with either ClC-7-GFP or ClC-7^{Y715C}-GFP 12 h before being challenged with IgG-coated sRBCs. Imaging to assess the degradation of the engulfed targets was performed 4 h after phagocytosis, using anti-IgG antibodies to visualize the opsonin. **(B)** Mean sRBC volumes measured 4 h after phagocytosis in experiments like those illustrated in A. Data from three independent experiments, each representing >25 phagosomes.

modulation of PIKfyve kinase activity alone cannot fully explain the effects of Snx10.

Two additional modes of action can be contemplated. First, Snx10 may prevent accumulation of PI(3,5)P_2 in late (endo)lysosomal compartments by stimulating its degradation, conceivably by activating lipid phosphatase(s). The reported association of Snx10 with PIKfyve (Bao et al., 2021) may in fact occur via a binding partner, Fig4, which is a phosphoinositide 5-phosphatase, that is also an integral part of the conserved PIKfyve heteromeric complex (Lees et al., 2020). While regulation of PI(3,5)P_2 phosphatase activity in lysosomes cannot be ruled out, we regard this mechanism as unlikely because Snx10 is primarily present in earlier endosomal compartments and because overexpression of Snx10 reduced the lysosomal accumulation of PI(3)P when PIKfyve was inhibited (Fig. 6 H and Fig. S4 F); this observation cannot be readily explained by inhibition of a PI(3,5)P_2 phosphatase, inasmuch as this phosphoinositide was absent following treatment with YM201636.

The second alternative, which we favor, implicates the availability of PI(3)P in late (endo)lysosomal compartments, where it determines the rate of formation of PI(3,5)P_2. In this scenario, Snx10 restricts the delivery of PI(3)P to (Rab7-positive) late compartments. This could result from reduced availability of PI(3)P in early, upstream compartments, or from its impaired delivery to the lysosomal compartment. Indeed, given its ability to bind PI(3)P through its PX domain, Snx10 may directly scavenge a fraction of the phosphoinositide in the early endosomes. However, the vacuolating effect of Snx10 overexpression required not only its PX domain but also its C-terminal region (Yao et al., 2009), ruling out mere PI(3)P scavenging as the responsible mechanism. Direct scavenging of PI(3)P would also be expected to limit the ability of mRFP-FKBP-PIKfyve^{CC} to generate PI(3,5)P_2 when recruited to the early Rab5 compartment; this, however, was not the case (Fig. 6 F; and Fig. S4, C and D). Moreover, scavenging fails to explain the observed net accumulation of PI(3)P detected by mass spectrometry in Snx10 KO cells (Fig. 5 B). Alternatively, Snx10 may negatively regulate the generation of PI(3)P in early compartments by modulating the activity and/or the traffic of the class III PI3-kinase Vps34, which is the major source of vesicular PI(3)P in our cells (Fig. S1 H). However, we find both possibilities to be unlikely. An inhibitory role for Snx10 on Vps34 kinase activity conflicts with the observation that loss of Snx10 led to a modest decrease in PI(3)P levels on early Rab5 compartments (Fig. S5, A and B), where the opposite effect would be expected. Additionally, recruitment of mRFP-FKBP-PIKfyve^{CC} to Rab5 compartments resulted in virtually complete solubilization of the PX-GFP probe in both WT and Snx10 KO cells (Fig. S5, I and J), which suggests that early Rab5-positive endosomes are the source of all vesicular PI(3)P detected in the Snx10 KO cells, and that Vps34 resides exclusively in that compartment. These observations together argue against Snx10 negatively regulating Vps34 activity and/or traffic. It is also noteworthy that the lysosomal swelling observed in Snx10-overexpressing cells (e.g., Fig. 5 G) was not replicated in cells where PI(3)P in the early endosomal compartments was acutely depleted by inhibition of Vps34 (see Fig. S5 H).

For these reasons, we feel that rather than altering the availability of PI(3)P in early compartments, Snx10 may control its delivery to late endosomes and lysosomes. Our data appear consistent with this mode of action: First, more PI(3)P, as detected by the $p40_{phox}^{PX}$ probe, was found in Rab7-positive compartments when Snx10 was deleted (Fig. 6 G and Fig. S4 E). Snx10 overexpression also affected the amount of PI(3)P accumulated in Rab7-positive compartments in response to inhibition of PIKfyve (Fig. 6 H and Fig. S4 F). In addition, when inducing recruitment of FKBP-PIKfyve^{CC}, the deletion of Snx10 altered the amount of PI(3,5)P_2 formed in Rab7-, but not in Rab5-positive compartments (Fig. 6, E and F; and Fig. S4, A–D).

The exact mechanism whereby Snx10 controls PI(3)P delivery to late compartments is still unclear. Snx10 may be directly involved in the generation or maintenance of putative intermediate compartments that delay the delivery of early endosomal PI(3)P to late compartments, or could instead indirectly control delivery by recruiting PI(3)P phosphatases—such as myotubularins—to early and/or intermediate compartments and accelerate PI(3)P turnover. Indeed, loss of Snx10 leads to an overall increase in PI(3)P in our macrophages (Fig. 5 B). Future follow-up studies could differentiate these alternatives.

In summary, we found that Snx10 regulates the activity of ClC-7 indirectly by influencing the availability of PI(3,5)P_2 in the lysosomal compartment. Collectively, our data suggest that Snx10 controls the rate of delivery of PI(3)P to late compartments, where it is converted to PI(3,5)P_2 by PIKfyve. This interpretation is consistent with the proposed function of sorting nexins in the regulation of membrane traffic (Carlton et al., 2004; Elson et al., 2021; Worby and Dixon, 2002). The well-established roles of Snx10 in bone and neuronal homeostasis as well as development (Aker et al., 2012; Pangrazio et al., 2013; Stattin et al., 2017) may very well result from similar effects on phosphoinositide traffic and metabolism.

Materials and methods

Cell culture

RAW 264.7 and HeLa cells were obtained from and authenticated by the American Type Culture Collection. ClC-7 KO RAW 264.7 macrophages were generated previously (Wu et al., 2023). Cell lines were grown in DMEM + 5% FBS at 37°C under 5% CO_2.

Generation of Snx10 KO clones

RAW 264.7 cells were seeded on 6-well tissue culture plates for 24 h and then transfected with a Guaranteed Predesigned CRISPR gRNA p01 plasmid (Sigma-Aldrich) against Snx10 (MMPD0000084302) containing Cas9 and GFP to indicate transfection. Cells were then incubated with propidium iodide, and live, transfected cells (GFP positive and propidium iodide negative) were sorted by FACS into 96-well tissue culture plates. After expansion, KO clones were verified by immunoblotting.

Plasmids

All plasmids utilized in this study are summarized in Table S1. The generation of ClC-7^{Y715C}-GFP from rat ClC-7-GFP was accomplished with site-directed mutagenesis using the In-Fusion HD EcoDry Cloning Kit (121416; Takara), and the following forward and reverse primers (5′ – 3′): 5′-AAAGACTTTCGCGATGCC T**G**CCCACGCTTC-3′, 5′-GAAGCGTGGGCAGGCATCGCGAAAGTC TTT-3′ (point mutation in bold). Snx10-mCherry was constructed from Snx10-GFP (MG51516-ACG; Sinobiological) by PCR amplifying the Snx10-GFP ORF with the following primers (5′ – 3′): 5′-GATCTCGAGCTCAAGCTTCGATGTTCCCAGAACAGCAGA AAG-3′, 5′-GGTACCGTCGACTGCAGAATTTTGGACTCCTGCAGA GCTGGGCTC-3′, and inserted into a pmCherry N1 vector (Clontech) linearized with *EcoRI* by Gibson assembly (New England Biolabs). Snx10^{R51Q}-GFP was generated from Snx10-GFP by site-directed mutagenesis using the Phusion High-Fidelity DNA Polymerase (F530S; Thermo Fisher Scientific), and the following forward and reverse primers (5′ – 3′): 5′-CAGAGAAGG TATAGAGAGTTCGTG-3′, 5′-TACACAAGATGTTTTCATTGTAA-3′. The design, assembly, and validation of the mRFP-FKBP-PIKfyve^{CC} and mRFP-FKBP-PIKfyve^{CC} K1877A recruitable enzymes, as well as the NES-mNG-NES-(2x)*Dd*SnxA^{PX} probe, are detailed in a complementary study (Pemberton et al., 2025), while plasmids iRFP-FRB-Rab5 (#51612; Addgene) and iRFP-FRB-Rab7 (#51613; Addgene) have been described previously (Hammond et al., 2014).

Reagents and antibodies

Commercially available reagents utilized in this study are summarized in Table S2. Antibodies utilized in this study are summarized in Table S3. All antibodies were resuspended in 1X TBS solution with 0.05% Tween 20 (TBST) supplemented with 5% BSA. All fluorescent secondary antibodies conjugated with AlexaFluor-488, -555, -647, or -HRP were obtained from Jackson ImmunoResearch.

sRBC preparation

IgG-opsonized sRBCs were prepared as described previously (Wu et al., 2023). Briefly, 30 µl of a 10% suspension of sRBCs were resuspended in 500 µl of PBS. Cells were washed thrice with PBS, then coated with IgG by incubating for 30 min with 1.5 µl of anti-sRBC IgG fraction, shaking at 300 rpm at 37°C. sRBCs were then washed thrice with PBS and utilized.

Immunoblotting

WT, ClC-7 KO, and Snx10 KO RAW 264.7 macrophages were grown on 6-well tissue culture plates for 18 h prior to harvesting. Cells were subsequently collected on ice and lysed in 100 µl radioimmunoprecipitation assay buffer containing protease and phosphatase inhibitors. Protein concentrations were measured using the BCA assay (Pierce), and samples were diluted in Laemmli buffer containing 10% 2-mercaptoethanol and boiled for 5 min at 95°C. Samples were then separated on 10% SDS-PAGE gels, transferred onto a polyvinylidene difluoride membrane, and blocked overnight in TBST and 5% BSA at 4°C. The blocked membranes were then incubated with primary antibodies in TBST containing 5% BSA for 1 h at room temperature; unless otherwise indicated all antibodies were used at a 1:1,000 dilution. The membrane was then washed thrice with TBST and subsequently incubated for 1 h at room temperature with secondary antibody conjugated to HRP (diluted 1:2,000 unless otherwise indicated), before being washed thrice with TBST.

Blots were developed using the ECL Prime western blot detection reagent and visualized with a ChemiDoc MP Imaging System (BioRad) and Image Lab software 5.2.1 (BioRad).

Immunofluorescence

WT, ClC-7 KO, and Snx10 KO RAW 264.7 macrophages were seeded on 18-mm coverslips in 12-well tissue culture plates 18 h prior to experimentation. After experimental treatment, cells were fixed at room temperature in 3% paraformaldehyde for 10 min, permeabilized in 0.1% Triton X-100 for 10 min, and blocked in 5% BSA for 30 min. Subsequently, the cells were incubated with the indicated primary antibodies in 5% BSA for 1 h, washed thrice with 1X PBS, and then incubated with appropriate fluorescent secondary antibodies in 5% BSA for 1 h. Cells were then washed thrice with PBS and imaged.

Cathepsin C cleavage assay

WT and Snx10 KO RAW 264.7 cell lysates were separated by SDS-PAGE and probed with anti-cathepsin C and anti-vinculin antibodies. The percentage of mature cathepsin C was determined by calculating the ratio of the mature cathepsin C (≈25 kDa) over the total cathepsin C (sum of mature cathepsin C and pro-cathepsin C [≈55 kDa] bands). Signals were normalized to the amount of vinculin, used as loading control. Densitometric measurements were quantified using ImageJ.

DQ-BSA assay

RAW 264.7 macrophages were seeded on 18-mm coverslips in 12-well tissue culture plates 18 h prior to experimentation. Cells were then incubated with IgG-opsonized DQ-BSA–coated silica beads for 30 min prior to imaging. To generate labeled beads, the silica beads were incubated with DQ-BSA red (Molecular Probes) shaking at 950 rpm at room temperature for 2 h. Beads were subsequently washed thrice with 1X PBS to remove excess unbound DQ-BSA, then opsonized with human IgG at 37°C, shaking at 950 rpm for 30 min. Beads were then washed thrice more with excess 1X PBS prior to addition to cells. The fluorescence of the DQ-BSA signal from beads that were not internalized was used to subtract the background (baseline DQ-BSA signal) from all experimental samples.

Phagosome resolution

RAW 264.7 macrophages were seeded on 18-mm coverslips in 12-well tissue culture plates 18 h prior to experimentation. Subsequently, cells were challenged for 1 or 4 h with IgG-opsonized sRBC. In all cases, the cells were washed for 20 min after initial incubation with sRBC to ensure all unbound particles were removed. For visualization, cells were fixed, permeabilized, and stained for 30 min prior to imaging with fluorescent secondary antibodies against the opsonizing antibody and with fluorescent phalloidin to visualize the sRBC target and macrophage actin, respectively. Stained actin was used to identify cell outlines for quantification and segmentation purposes and is outlined in representative images.

Transient plasmid DNA transfection

RAW 264.7 macrophages were seeded on 18-mm coverslips in 12-well tissue culture plates at a concentration of ∼2 × 10^5 cells 18 h prior to transfection. Cells were then transfected with the desired plasmid DNA using FuGENE HD (Promega) transfection reagent at a ratio of 3:1 (FuGENE to DNA), using 1 µg of total plasmid DNA per condition. Medium was replaced 4 h after transfection, and cells were imaged 8–10 h later.

HeLa cells were seeded on 18-mm coverslips in 12-well tissue culture plates at a concentration of ∼1.5 × 10^5 cells 18 h prior to transfection. Cells were then transfected with the desired plasmid DNA using FuGENE 6 (Promega) reagent at a ratio of 3:1 (FuGENE to DNA), with 1 µg of total plasmid DNA per condition. Medium was replaced 5 h after transfection, and cells were imaged 12–18 h later.

Labeling of phagolysosomes by dextran pulse chase

RAW 264.7 macrophages seeded on 18-mm coverslips in 12-well tissue culture plates were incubated ("pulsed") for 16 h with 100 µg/ml of fluorescently labeled 10 kDa dextran, then washed thrice ("chased") with fresh medium 1 h prior to experimentation to allow for the delivery of the labeled dextran from earlier endocytic compartments to lysosomes.

Ratiometric pH measurements

WT and Snx10 KO RAW 264.7 macrophages were seeded on 18-mm coverslips in 12-well tissue culture plates 18 h prior to experimentation. Macrophages were incubated with FITC-conjugated IgG-opsonized sRBC or zymosan for 1 h, which were prepared by reacting sRBC or zymosan with FITC as described previously (Wu et al., 2023), then subsequently imaged to determine the steady-state phagosomal pH. FITC was excited at 490 nm, which emits at 520 nm in a pH-dependent manner, as well as at 440 nm, which emits at 520 nm in a manner that is much less sensitive to pH. Cells were then sequentially bathed in standard pH buffers (143 mM KCl, 5 mM glucose, 1 mM $MgCl_2$, 1 mM $CaCl_2$, and 20 mM Hepes) of pH 7.5, 6.5, 5.5, and 4.5 containing also 10 µM nigericin and 5 µM monensin for 10 min each. The 490 nm/440 nm fluorescence ratio was collected at each pH to construct a calibration curve, fitted by the least squares method, correlating the mean fluorescence ratio (background subtracted) against the known pH values. This was ultimately utilized to convert the recorded fluorescence ratio values to pH values. A standard pH curve was generated for each experimental condition.

Determinations of organellar [Cl^-]

Colorimetric determinations of sucrosomal [Cl^-]

RAW 264.7 macrophages were incubated overnight in culture medium containing 50 mM sucrose prior to experimentation. Cells were visually confirmed to have formed sucrosomes by the formation of large, distended vacuoles clearly observable by brightfield microscopy.

Colorimetric determination of Cl^- was adapted from a previous report (Zall et al., 1956). Sucrosome-containing WT, ClC-7 KO, and Snx10 KO cells were incubated in either chloride-containing buffer (130 mM NaCl, 3 mM KCl, 1 mM $MgCl_2$, 1 mM $CaCl_2$, 10 mM glucose, and 20 mM Hepes, pH 7.4) or in nitrate containing buffer (130 mM $NaNO_3$, 3 mM KNO_3, 1 mM $Mg[NO_3]_2$, 1 mM $Ca[NO_3]_2$, 10 mM glucose, and 20 mM Hepes, pH 7.4) for 2 h to deplete cell chloride. Where indicated, the cells

were treated with 500 nM CCA for 30 min. Cells were subsequently washed thrice in ice-cold gluconate buffer (140 mM Na-gluconate, 10 mM glucose, and 20 mM HEPES, pH 7.4), then treated with 3 mM ATP for 30 s, and washed rapidly thrice in ice-cold gluconate buffer prior to overnight lysis in 1% HNO_3. Lysates were then centrifuged at 10,000 × *g* for 10 min to remove particulate material, and the supernatant was mixed in equal parts with a mercuric solution (1 part 0.417% mercuric thiocyanate in methanol, 1 part 20.2% ferric nitrate solution, and 13 parts water) in a 96-well plate. The absorbance at 490 nm is indicative of the concentration of Cl^- in the sample and was measured using a microplate reader (Biotek, Epoch Microplate Spectrophotometer). [Cl^-] standards were used to construct a standard curve. To determine sucrosomal [Cl^-], cell number was determined in parallel samples using a Coulter counter (Beckman Coulter Life Sciences, Multisizer 4), and sucrosomal volume was determined by imaging parallel samples that had been pulsed overnight with AlexaFluor-647–conjugated 10 kDa dextran that was chased for 1 h with fresh medium to ensure delivery to sucrosomes. Sucrosomal volume was then calculated using Imaris (Oxford Instruments) software. To ensure their predominant contribution, the mean sucrosomal volume was verified to be >60% of the mean total cell volume of each replicate prior to [Cl^-] determinations.

Colorimetric determinations of enlarged endolysosomal [Cl^-]

RAW 264.7 macrophages were co-incubated with 100 nM YM201636 for 30 min prior to experimentation to enlarge endolysosomes, which was confirmed by the formation of large vacuoles in all cells by brightfield microscopy. Cells were subsequently processed exactly as described above with the determinations of sucrosomal [Cl^-].

Generation and use of fluorescent chloride-sensitive 10 kDa BAC-dextran

The succinimidyl ester of the [Cl^-]-sensitive fluorescent molecule BAC-succinimidyl ester was conjugated to 10 kDa amino-dextran by co-incubating both reagents in borate buffer (50 mM borate, pH 8.5) for 2 h at room temperature (25°C) while shaking at 600 rpm away from light. The resulting mixture was subsequently dialyzed for 24 h (Slide-A-Lyzer Dialysis Cassettes, 2K MWCO) against PBS at 4°C with gentle stirring, changing the PBS every 8 h, to generate 10 kDa BAC-dextran.

To estimate their lysosomal [Cl^-], WT, ClC-7 KO, or Snx10 KO RAW 264.7 macrophages were pulsed overnight with 10 kDa BAC-dextran and chased for 1 h prior to experimentation; where indicated, WT, ClC-7 KO, and Snx10 KO cells were treated with CCA or bathed in nitrate medium devoid of chloride. To normalize for differential uptake of the indicator, cells were simultaneously pulsed with AlexaFluor-647–conjugated 10 kDa dextran, which is insensitive to [Cl^-] changes. The fluorescence ratio of the 647-dextran to the BAC-dextran was quantified microscopically as described below.

Determination of phospholipid levels by mass spectrometry

Cell pellets were frozen and thawed once and then mixed with 50 µl of chloroform/methanol (1:9) solution containing 1 nmol of C8:0/C8:0 PI(4,5)P_2 (as an absorption inhibitor) and 10 pmol of heptadecanoyl/arachidonoyl (C17:0/C20:4) species of each phosphoinositide class (as an internal standard). 450 µl of formic acid was added and vortexed, followed by the addition of 4.5 ml of chloroform/methanol (1:1) and vortexing. A 50 µl aliquot was transferred to a separate tube for measurement of other glycerophospholipids. The rest was applied to a DEAE-Sepharose column that had been equilibrated with chloroform for the preparation of samples for phosphoinositide measurement. The column was washed with 3 ml of chloroform/methanol (1:1) solution, followed by 2 ml of chloroform/methanol/28% ammonium hydroxide/glacial acetic acid (200:100:3:0.9) solution. Phosphoinositides were eluted with 2 ml of chloroform/methanol/concentrated HCl/ultrapure water (12:12:1:1) solution. The eluate was collected in a new tube, and 1,130 µl of 120 mM NaCl was added and vigorously vortexed. After centrifugation (1,200 × *g* for 3 min), the lower phase was transferred to another tube. The derivatization of phosphoinositides by methylation was performed as described in our previous publication (Morioka et al., 2022). Phosphoinositide regioisomer measurement by chiral column chromatography and mass spectrometry was conducted using a triple quadrupole mass spectrometer QTRAP 6500 (SCIEX) combined with a Nexera XR HPLC/Autosampler system (Shimadzu). A sample in acetonitrile (10 µl) was injected, and phosphoinositides were separated using a CHIRALPAK IC-3 column (cellulose tris[3,5-dichlorophenylcarbamate], 2.1 × 250 mm, 3 µm; DAICEL) at 23°C. The LC was operated at a flow rate of 100 µl/min with a gradient as follows: 40% mobile phase A (methanol/5 mM ammonium acetate) and 60% mobile phase B (acetonitrile/5 mM ammonium acetate) were held for 1 min, linearly increased to 70% mobile phase A over 2 min and held at 70% mobile phase A for 7 min. Table S4 lists the MRM transitions (pairs of m/z values of precursor and product ions) used for the measurements of phosphoinositide molecular species. Analyst 1.6.3 (SCIEX) was used for data acquisition and processing. MultiQuant (SCIEX) was used for manual data evaluation for peak integration. No background subtraction was performed. Gaussian smoothing width was 1.0 points. The sample peak area value was divided by the corresponding internal standard peak area value for quantification.

For general phospholipid analysis, PA, PG, PC, PE, and PS were separated by reverse-phase column chromatography and subjected to mass spectrometry for measurement. To the 50 µl of cellular lipid extract solution that had been previously separated as described above, 10 pmol each of C15:0/C18:1-d7 PC, C15:0/C18:1-d7 PE, C15:0/C18:1 PA, C12:0/C13:0 PG, and C17:0/C14:1 PS were added as internal standards. The samples were mixed with 1.5 ml of chloroform/methanol/concentrated HCl/ultrapure water (12:12:1:1) solution and 850 µl of 120 mM NaCl and vigorously vortexed. After centrifugation (1,200 × *g* for 3 min), the lower phase was transferred to another tube and subjected to a methylation reaction as described previously, except that the resultant dried phospholipids were dissolved in 400 µl of methanol/ultrapure water (3:1) solution, and 10 µl was used for measurement. A Nexera X2 HPLC system (Shimadzu) equipped with an HTC PAL autosampler (CTC Analytics) was used for column chromatography. Separation of the phospholipid classes

used a COSMOCORE 2.6C18 column (2.1 × 150 mm, 2.6 µm; Nacalai Tesque) at 60°C, with the mobile phase containing isopropanol/acetonitrile/1 M ammonium acetate (160:40:1) (A) and acetonitrile/ultrapure water/1 M ammonium acetate (160:40:1) (B). The gradient program was as follows: 0–1 min = 30% A, 1–3 min = 30–90% A, 3–7.5 min = 90% A,and 7.5–12 min = 30% A. A QTRAP5500 (SCIEX) was used for electrospray ionization MS/MS analysis. Measurement of the phospholipid species was achieved through multiple reaction monitoring using a preset list of mass-to-charge ratio values shown in Table S5.

Microscopy

Microscopy was performed on a spinning-disk system (Quorum Technologies, Inc.), comprised of an Axiovert 200 M microscope (Zeiss), cooled CCD camera (ORCA-Fusion BT, Hamamatsu), five-line laser module (Spectral Applied Research) with 405-, 443-, 491-, 561- and 655-nm lines, and a filter wheel (MAC5000; Ludl). The microscope was operated using Volocity v6.3 software (Perkin Elmer). Images were acquired with a 63×/1.4 NA oil objective (Zeiss). Ratiometric pH imaging was performed on a microscopy system that consists of an Axio Observer microscope (Zeiss), cooled CCD camera (Evolve 512; Photometrics), and a fluorescent light source (HXP 120V; Zeiss). Ratiometric imaging of FITC was performed using 470/40-nm and 436/20-nm excitation filters. The microscope was operated using ZEN 2 blue edition software (Zeiss), and images were acquired with a 63×/1.4 NA oil objective (Zeiss).

Image analysis

Image processing and analyses were performed using Volocity v6.3 software (Perkin Elmer). Fluorescence intensities of microscopy images were quantified using Volocity v6.3 and ImageJ. Volume of dextran-labeled sucrosomes was determined with Imaris (Oxford Instruments). Pseudocolor representations were created in ImageJ using the "Fire" look-up table function and were used to visualize the relative fluorescence intensity of DQ-BSA–coated silica beads contained within phagosomes and the inverted "Magenta hot" look-up table to visualize phagosomal resolution.

General methodology and statistics

Data are presented as means ± SD. Statistical significance of data was determined using unpaired Student's *t* tests with $P < 0.05$ considered significant. Statistical analyses were performed in GraphPad Prism 9.5.1 and Microsoft Excel. Each experiment was performed at least three times.

Online supplemental material

Fig. S1 characterizes the identity and morphology of endolysosomes from macrophages that were subjected to the various treatments and genetic ablations used in this study. Fig. S2 details the content of PC, PE, PS, PG, PA, PI, PI4P, PI(4,5)P_2, and PIP_3 in WT and Snx10 KO macrophage lysates, determined by phosphoinositide regioisomer measurement by chiral column chromatography and mass spectrometry. Fig. S3 characterizes the identity, morphology, and chloride content of maximally swollen endolysosomes in macrophages treated with PIKfyve inhibitors. Fig. S4 encompasses the representative microscopy images of the experiments used to quantify Fig. 6, E–H. Fig. S5 characterizes the localization of PI(3)P and of the PI(3)P-effector EEA1 relative to early and late endosomes in WT and Snx10 KO macrophages, as well as illustrating the depletion of PI(3)P in early endocytic compartments upon recruitment of active PIKfyve^{CC}. Table S1 shows the plasmids. Table S2 shows the reagents. Table S3 shows the antibodies. Table S4 shows the MRM transitions for phosphoinositides. Table S5 shows the MRM transitions for PC, PE, PA, PG, and PS.

Data availability

Original data are available from the corresponding authors upon reasonable request.

Acknowledgments

The authors thank Dr. Thomas Jentsch (Leibniz-Forschungsinstitut für Molekulare Pharmakologie and Max-Delbrück-Centrum für Molekulare Medizin, Berlin, Germany) for the anti–ClC-7 antibody.

J.Z. Wu is funded by a Natural Sciences and Engineering Research Council of Canada (NSERC) Scholarship. S. Grinstein is supported by a Project Grant PJT-169180 from CIHR. S.A. Freeman is supported by a Discovery Grant RGPIN-2022-04485 from NSERC and holds a Canada Research Chair from CIHR.

Author contributions: J.Z. Wu: conceptualization, data curation, formal analysis, funding acquisition, investigation, methodology, validation, visualization, and writing—original draft, review, and editing. J.G. Pemberton: conceptualization, methodology, resources, and writing—review and editing. S. Morioka: investigation. J. Sasaki: investigation. P. Bablani: investigation and resources. T. Sasaki: investigation, methodology, resources, supervision, and writing—original draft. T. Balla: funding acquisition, project administration, resources, and writing—review and editing. S. Grinstein: conceptualization, formal analysis, funding acquisition, project administration, supervision, and writing—original draft, review, and editing. S.A. Freeman: conceptualization, funding acquisition, methodology, project administration, resources, supervision, visualization, and writing—original draft, review, and editing.

Disclosures: The authors declare no competing interests exist.

Submitted: 22 August 2024
Revised: 9 February 2025
Accepted: 6 March 2025

References

Aghajari, N., G. Feller, C. Gerday, and R. Haser. 2002. Structural basis of alpha-amylase activation by chloride. *Protein Sci.* 11:1435–1441. https://doi.org/10.1110/ps.0202602

Aker, M., A. Rouvinski, S. Hashavia, A. Ta-Shma, A. Shaag, S. Zenvirt, S. Israel, M. Weintraub, A. Taraboulos, Z. Bar-Shavit, and O. Elpeleg. 2012. An SNX10 mutation causes malignant osteopetrosis of infancy. *J. Med. Genet.* 49:221–226. https://doi.org/10.1136/jmedgenet-2011-100520

Bao, W., X. Liu, Y. You, H. Hou, X. Wang, S. Zhang, H. Li, G. Feng, X. Cao, H. Jiang, et al. 2021. Targeting sorting nexin 10 improves mouse colitis via

inhibiting PIKfyve-mediated TBK1/c-Rel signaling activation. *Pharmacol. Res.* 169:105679. https://doi.org/10.1016/j.phrs.2021.105679

Barnea-Zohar, M., S.E. Winograd-Katz, M. Shalev, E. Arman, N. Reuven, L. Roth, O. Golani, M. Stein, F. Thalji, M. Kanaan, et al. 2021. An SNX10-dependent mechanism downregulates fusion between mature osteoclasts. *J. Cell Sci.* 134:jcs254979. https://doi.org/10.1242/jcs.254979

Bright, N.A., L.J. Davis, and J.P. Luzio. 2016. Endolysosomes are the principal intracellular sites of acid hydrolase activity. *Curr. Biol.* 26:2233–2245. https://doi.org/10.1016/j.cub.2016.06.046

Bucci, C., P. Thomsen, P. Nicoziani, J. McCarthy, and B. van Deurs. 2000. Rab7: A key to lysosome biogenesis. *Mol. Biol. Cell.* 11:467–480. https://doi.org/10.1091/mbc.11.2.467

Cai, R., O. Scott, G. Ye, T. Le, E. Saran, W. Kwon, S. Inpanathan, B.A. Sayed, R.J. Botelho, A. Saric, et al. 2024. Pressure sensing of lysosomes enables control of TFEB responses in macrophages. *Nat. Cell Biol.* 26:1247–1260. https://doi.org/10.1038/s41556-024-01459-y

Carlton, J., M. Bujny, B.J. Peter, V.M. Oorschot, A. Rutherford, H. Mellor, J. Klumperman, H.T. McMahon, and P.J. Cullen. 2004. Sorting nexin-1 mediates tubular endosome-to-TGN transport through coincidence sensing of high- curvature membranes and 3-phosphoinositides. *Curr. Biol.* 14:1791–1800. https://doi.org/10.1016/j.cub.2004.09.077

Carpaneto, A., A. Boccaccio, L. Lagostena, E. Di Zanni, and J. Scholz-Starke. 2017. The signaling lipid phosphatidylinositol-3,5-bisphosphate targets plant CLC-a anion/H^+ exchange activity. *EMBO Rep.* 18:1100–1107. https://doi.org/10.15252/embr.201643814

Chadwick, S.R., S. Grinstein, and S.A. Freeman. 2021a. From the inside out: Ion fluxes at the centre of endocytic traffic. *Curr. Opin. Cell Biol.* 71:77–86. https://doi.org/10.1016/j.ceb.2021.02.006

Chadwick, S.R., J.Z. Wu, and S.A. Freeman. 2021b. Solute transport controls membrane tension and organellar volume. *Cell. Physiol. Biochem.* 55:1–24. https://doi.org/10.33594/000000318

Chen, Y., B. Wu, L. Xu, H. Li, J. Xia, W. Yin, Z. Li, D. Shi, S. Li, S. Lin, et al. 2012. A SNX10/V-ATPase pathway regulates ciliogenesis in vitro and in vivo. *Cell Res.* 22:333–345. https://doi.org/10.1038/cr.2011.134

Cigic, B., and R.H. Pain. 1999. Location of the binding site for chloride ion activation of cathepsin C. *Eur. J. Biochem.* 264:944–951. https://doi.org/10.1046/j.1432-1327.1999.00697.x

De Duve, C., and R. Wattiaux. 1966. Functions of lysosomes. *Annu. Rev. Physiol.* 28:435–492. https://doi.org/10.1146/annurev.ph.28.030166.002251

Delamarre, L., M. Pack, H. Chang, I. Mellman, and E.S. Trombetta. 2005. Differential lysosomal proteolysis in antigen-presenting cells determines antigen fate. *Science.* 307:1630–1634. https://doi.org/10.1126/science.1108003

Elson, A., M. Stein, G. Rabie, M. Barnea-Zohar, S. Winograd-Katz, N. Reuven, M. Shalev, J. Sekeres, M. Kanaan, J. Tuckermann, and B. Geiger. 2021. Sorting nexin 10 as a key regulator of membrane trafficking in bone-resorbing osteoclasts: Lessons learned from osteopetrosis. *Front. Cell Dev. Biol.* 9:671210. https://doi.org/10.3389/fcell.2021.671210

Farfel-Becker, T., J.C. Roney, X.T. Cheng, S. Li, S.R. Cuddy, and Z.H. Sheng. 2019. Neuronal soma-derived degradative lysosomes are continuously delivered to distal axons to maintain local degradation capacity. *Cell Rep.* 28:51–64.e4. https://doi.org/10.1016/j.celrep.2019.06.013

Gayle, S., S. Landrette, N. Beeharry, C. Conrad, M. Hernandez, P. Beckett, S.M. Ferguson, T. Mandelkern, M. Zheng, T. Xu, et al. 2017. Identification of apilimod as a first-in-class PIKfyve kinase inhibitor for treatment of B-cell non-Hodgkin lymphoma. *Blood.* 129:1768–1778. https://doi.org/10.1182/blood-2016-09-736892

Gillooly, D.J., I.C. Morrow, M. Lindsay, R. Gould, N.J. Bryant, J.M. Gaullier, R.G. Parton, and H. Stenmark. 2000. Localization of phosphatidylinositol 3-phosphate in yeast and mammalian cells. *EMBO J.* 19:4577–4588. https://doi.org/10.1093/emboj/19.17.4577

Hammond, G.R., M.P. Machner, and T. Balla. 2014. A novel probe for phosphatidylinositol 4-phosphate reveals multiple pools beyond the Golgi. *J. Cell Biol.* 205:113–126. https://doi.org/10.1083/jcb.201312072

Honey, K., and A.Y. Rudensky. 2003. Lysosomal cysteine proteases regulate antigen presentation. *Nat. Rev. Immunol.* 3:472–482. https://doi.org/10.1038/nri1110

Hu, W., C. Chi, K. Song, and H. Zheng. 2023. The molecular mechanism of sialic acid transport mediated by Sialin. *Sci. Adv.* 9:eade8346. https://doi.org/10.1126/sciadv.ade8346

Ikonomov, O.C., D. Sbrissa, and A. Shisheva. 2001. Mammalian cell morphology and endocytic membrane homeostasis require enzymatically active phosphoinositide 5-kinase PIKfyve. *J. Biol. Chem.* 276:26141–26147. https://doi.org/10.1074/jbc.M101722200

Jefferies, H.B., F.T. Cooke, P. Jat, C. Boucheron, T. Koizumi, M. Hayakawa, H. Kaizawa, T. Ohishi, P. Workman, M.D. Waterfield, and P.J. Parker. 2008. A selective PIKfyve inhibitor blocks PtdIns(3,5)P(2) production and disrupts endomembrane transport and retroviral budding. *EMBO Rep.* 9:164–170. https://doi.org/10.1038/sj.embor.7401155

Kanai, F., H. Liu, S.J. Field, H. Akbary, T. Matsuo, G.E. Brown, L.C. Cantley, and M.B. Yaffe. 2001. The PX domains of p47phox and p40phox bind to lipid products of PI(3)K. *Nat. Cell Biol.* 3:675–678. https://doi.org/10.1038/35083070

Kasper, D., R. Planells-Cases, J.C. Fuhrmann, O. Scheel, O. Zeitz, K. Ruether, A. Schmitt, M. Poët, R. Steinfeld, M. Schweizer, et al. 2005. Loss of the chloride channel ClC-7 leads to lysosomal storage disease and neurodegeneration. *EMBO J.* 24:1079–1091. https://doi.org/10.1038/sj.emboj.7600576

Kim, G.H., R.M. Dayam, A. Prashar, M. Terebiznik, and R.J. Botelho. 2014. PIKfyve inhibition interferes with phagosome and endosome maturation in macrophages. *Traffic.* 15:1143–1163. https://doi.org/10.1111/tra.12199

Kornak, U., D. Kasper, M.R. Bösl, E. Kaiser, M. Schweizer, A. Schulz, W. Friedrich, G. Delling, and T.J. Jentsch. 2001. Loss of the ClC-7 chloride channel leads to osteopetrosis in mice and man. *Cell.* 104:205–215. https://doi.org/10.1016/S0092-8674(01)00206-9

Lees, J.A., P. Li, N. Kumar, L.S. Weisman, and K.M. Reinisch. 2020. Insights into lysosomal PI(3,5)P_2 homeostasis from a structural-biochemical analysis of the PIKfyve lipid kinase complex. *Mol. Cell.* 80:736–743.e4. https://doi.org/10.1016/j.molcel.2020.10.003

Leisle, L., C.F. Ludwig, F.A. Wagner, T.J. Jentsch, and T. Stauber. 2011. ClC-7 is a slowly voltage-gated 2Cl(−)/1H(+)-exchanger and requires Ostm1 for transport activity. *EMBO J.* 30:2140–2152. https://doi.org/10.1038/emboj.2011.137

Leray, X., J.K. Hilton, K. Nwangwu, A. Becerril, V. Mikusevic, G. Fitzgerald, A. Amin, M.R. Weston, and J.A. Mindell. 2022. Tonic inhibition of the chloride/proton antiporter ClC-7 by PI(3,5)P2 is crucial for lysosomal pH maintenance. *Elife.* 11:e74136. https://doi.org/10.7554/eLife.74136

Lo, C.H., and J. Zeng. 2023. Defective lysosomal acidification: A new prognostic marker and therapeutic target for neurodegenerative diseases. *Transl. Neurodegener.* 12:29. https://doi.org/10.1186/s40035-023-00362-0

Löbel, M., S.P. Salphati, K. El Omari, A. Wagner, S.J. Tucker, J.L. Parker, and S. Newstead. 2022. Structural basis for proton coupled cystine transport by cystinosin. *Nat. Commun.* 13:4845. https://doi.org/10.1038/s41467-022-32589-2

Lukacs, G.L., O.D. Rotstein, and S. Grinstein. 1990. Phagosomal acidification is mediated by a vacuolar-type H(+)-ATPase in murine macrophages. *J. Biol. Chem.* 265:21099–21107. https://doi.org/10.1016/S0021-9258(17)45332-4

Majumdar, A., E. Capetillo-Zarate, D. Cruz, G.K. Gouras, and F.R. Maxfield. 2011. Degradation of Alzheimer's amyloid fibrils by microglia requires delivery of ClC-7 to lysosomes. *Mol. Biol. Cell.* 22:1664–1676. https://doi.org/10.1091/mbc.e10-09-0745

McCartney, A.J., S.N. Zolov, E.J. Kauffman, Y. Zhang, B.S. Strunk, L.S. Weisman, and M.A. Sutton. 2014. Activity-dependent PI(3,5)P2 synthesis controls AMPA receptor trafficking during synaptic depression. *Proc. Natl. Acad. Sci. USA.* 111:E4896–E4905. https://doi.org/10.1073/pnas.1411117111

Melchionda, M., J.K. Pittman, R. Mayor, and S. Patel. 2016. Ca^{2+}/H^+ exchange by acidic organelles regulates cell migration in vivo. *J. Cell Biol.* 212:803–813. https://doi.org/10.1083/jcb.201510019

Metzner, L., K. Neubert, and M. Brandsch. 2006. Substrate specificity of the amino acid transporter PAT1. *Amino Acids.* 31:111–117. https://doi.org/10.1007/s00726-005-0314-6

Mony, V.K., S. Benjamin, and E.J. O'Rourke. 2016. A lysosome-centered view of nutrient homeostasis. *Autophagy.* 12:619–631. https://doi.org/10.1080/15548627.2016.1147671

Morioka, S., H. Nakanishi, T. Yamamoto, J. Hasegawa, E. Tokuda, T. Hikita, T. Sakihara, Y. Kugii, C. Oneyama, M. Yamazaki, et al. 2022. A mass spectrometric method for in-depth profiling of phosphoinositide regioisomers and their disease-associated regulation. *Nat. Commun.* 13:83. https://doi.org/10.1038/s41467-021-27648-z

Moriwaki, T., S. Terawaki, and T. Otomo. 2024. Impaired lysosomal acidity maintenance in acid lipase-deficient cells leads to defective autophagy. *J. Biol. Chem.* 300:105743. https://doi.org/10.1016/j.jbc.2024.105743

Muno, D., K. Ishidoh, T. Ueno, and E. Kominami. 1993. Processing and transport of the precursor of cathepsin C during its transfer into

lysosomes. *Arch. Biochem. Biophys.* 306:103–110. https://doi.org/10.1006/abbi.1993.1486

Nicoli, E.R., M.R. Weston, M. Hackbarth, A. Becerril, A. Larson, W.M. Zein, P.R. Baker II, J.D. Burke, H. Dorward, M. Davids, et al. 2019. Lysosomal storage and albinism due to effects of a de novo CLCN7 variant on lysosomal acidification. *Am. J. Hum. Genet.* 104:1127–1138. https://doi.org/10.1016/j.ajhg.2019.04.008

Ohkuma, S., Y. Moriyama, and T. Takano. 1982. Identification and characterization of a proton pump on lysosomes by fluorescein-isothiocyanate-dextran fluorescence. *Proc. Natl. Acad. Sci. USA.* 79:2758–2762. https://doi.org/10.1073/pnas.79.9.2758

Ostrowski, P.P., G.D. Fairn, S. Grinstein, and D.E. Johnson. 2016. Cresyl violet: A superior fluorescent lysosomal marker. *Traffic.* 17:1313–1321. https://doi.org/10.1111/tra.12447

Pangrazio, A., A. Fasth, A. Sbardellati, P.J. Orchard, K.A. Kasow, J. Raza, C. Albayrak, D. Albayrak, O.M. Vanakker, B. De Moerloose, et al. 2013. SNX10 mutations define a subgroup of human autosomal recessive osteopetrosis with variable clinical severity. *J. Bone Miner. Res.* 28: 1041–1049. https://doi.org/10.1002/jbmr.1849

Pemberton, J., I. Barlow-Busch, M. Jenkins, M. Parson, F. Sarnyai, S. Bektas, Y.J. Kim, J. Heuser, J. Burke, and T. Balla. 2025. An advanced toolset to manipulate and monitor subcellular phosphatidylinositol 3,5-bisphosphate. *J. Cell Biol.* https://doi.org/10.1083/jcb.202408158

Perera, R.M., and R. Zoncu. 2016. The lysosome as a regulatory hub. *Annu. Rev. Cell Dev. Biol.* 32:223–253. https://doi.org/10.1146/annurev-cellbio-111315-125125

Pillay, C.S., E. Elliott, and C. Dennison. 2002. Endolysosomal proteolysis and its regulation. *Biochem. J.* 363:417–429. https://doi.org/10.1042/bj3630417

Platt, F.M., A. d'Azzo, B.L. Davidson, E.F. Neufeld, and C.J. Tifft. 2018. Lysosomal storage diseases. *Nat. Rev. Dis. Primers.* 4:27. https://doi.org/10.1038/s41572-018-0025-4

Polovitskaya, M.M., T. Rana, K. Ullrich, S. Murko, T. Bierhals, G. Vogt, T. Stauber, C. Kubisch, R. Santer, and T.J. Jentsch. 2024. Gain-of-function variants in CLCN7 cause hypopigmentation and lysosomal storage disease. *J. Biol. Chem.* 300:107437. https://doi.org/10.1016/j.jbc.2024.107437

Rebsamen, M., L. Pochini, T. Stasyk, M.E. de Araújo, M. Galluccio, R.K. Kandasamy, B. Snijder, A. Fauster, E.L. Rudashevskaya, M. Bruckner, et al. 2015. SLC38A9 is a component of the lysosomal amino acid sensing machinery that controls mTORC1. *Nature.* 519:477–481. https://doi.org/10.1038/nature14107

Riazanski, V., G. Mauleon, A.M. Zimnicka, S. Chen, and D.J. Nelson. 2021. Phagosomal chloride dynamics in the alveolar macrophage. *iScience.* 25: 103636. https://doi.org/10.1016/j.isci.2021.103636

Roberts, R.L., M.A. Barbieri, K.M. Pryse, M. Chua, J.H. Morisaki, and P.D. Stahl. 1999. Endosome fusion in living cells overexpressing GFP-rab5. *J. Cell Sci.* 112:3667–3675. https://doi.org/10.1242/jcs.112.21.3667

Shin, H.R., and R. Zoncu. 2020. The lysosome at the intersection of cellular growth and destruction. *Dev. Cell.* 54:226–238. https://doi.org/10.1016/j.devcel.2020.06.010

Sonawane, N.D., J.R. Thiagarajah, and A.S. Verkman. 2002. Chloride concentration in endosomes measured using a ratioable fluorescent Cl- indicator: Evidence for chloride accumulation during acidification. *J. Biol. Chem.* 277:5506–5513. https://doi.org/10.1074/jbc.M110818200

Song, F., Y. Yi, C. Li, Y. Hu, J. Wang, D.E. Smith, and H. Jiang. 2018. Regulation and biological role of the peptide/histidine transporter SLC15A3 in Toll-like receptor-mediated inflammatory responses in macrophage. *Cell Death Dis.* 9:770. https://doi.org/10.1038/s41419-018-0809-1

Stattin, E.L., P. Henning, J. Klar, E. McDermott, C. Stecksen-Blicks, P.E. Sandström, T.G. Kellgren, P. Rydén, G. Hallmans, T. Lönnerholm, et al. 2017. SNX10 gene mutation leading to osteopetrosis with dysfunctional osteoclasts. *Sci. Rep.* 7:3012. https://doi.org/10.1038/s41598-017-02533-2

Styrt, B., and M.S. Klempner. 1982. Internal pH of human neutrophil lysosomes. *FEBS Lett.* 149:113–116. https://doi.org/10.1016/0014-5793(82)81083-1

Takatori, S., T. Tatematsu, J. Cheng, J. Matsumoto, T. Akano, and T. Fujimoto. 2016. Phosphatidylinositol 3,5-bisphosphate-rich membrane domains in endosomes and lysosomes. *Traffic.* 17:154–167. https://doi.org/10.1111/tra.12346

Tan, S., N. Sukumar, R.B. Abramovitch, T. Parish, and D.G. Russell. 2013. Mycobacterium tuberculosis responds to chloride and pH as synergistic cues to the immune status of its host cell. *PLoS Pathog.* 9:e1003282. https://doi.org/10.1371/journal.ppat.1003282

Vines, J.H., H. Maib, C.M. Buckley, A. Gueho, Z. Zhu, T. Soldati, D.H. Murray, and J.S. King. 2023. A PI(3,5)P2 reporter reveals PIKfyve activity and dynamics on macropinosomes and phagosomes. *J. Cell Biol.* 222: e202209077. https://doi.org/10.1083/jcb.202209077

Wartosch, L., J.C. Fuhrmann, M. Schweizer, T. Stauber, and T.J. Jentsch. 2009. Lysosomal degradation of endocytosed proteins depends on the chloride transport protein ClC-7. *FASEB J.* 23:4056–4068. https://doi.org/10.1096/fj.09-130880

Worby, C.A., and J.E. Dixon. 2002. Sorting out the cellular functions of sorting nexins. *Nat. Rev. Mol. Cell Biol.* 3:919–931. https://doi.org/10.1038/nrm974

Wu, J.Z., M. Zeziulia, W. Kwon, T.J. Jentsch, S. Grinstein, and S.A. Freeman. 2023. ClC-7 drives intraphagosomal chloride accumulation to support hydrolase activity and phagosome resolution. *J. Cell Biol.* 222:e202208155. https://doi.org/10.1083/jcb.202208155

Xu, H., and D. Ren. 2015. Lysosomal physiology. *Annu. Rev. Physiol.* 77:57–80. https://doi.org/10.1146/annurev-physiol-021014-071649

Yao, D., B. Wu, B. Qin, and D. Pei. 2009. PX domain and CD domain play different roles in localization and vacuolation of Sorting Nexin 10. *Chin. Sci. Bull.* 54:3965–3971. https://doi.org/10.1007/s11434-009-0529-0

Ye, L., L.R. Morse, L. Zhang, H. Sasaki, J.C. Mills, P.R. Odgren, G. Sibbel, J.R. Stanley, G. Wong, A. Zamarioli, and R.A. Battaglino. 2015. Osteopetrorickets due to Snx10 deficiency in mice results from both failed osteoclast activity and loss of gastric acid-dependent calcium absorption. *PLoS Genet.* 11:e1005057. https://doi.org/10.1371/journal.pgen.1005057

Zall, D.M., D. Fisher, and M.Q. Garner. 1956. Photometric determination of chlorides in water. *Anal. Chem.* 28:1665–1668. https://doi.org/10.1021/ac60119a009

Zhang, Q., Y. Li, Y. Jian, M. Li, and X. Wang. 2023. Lysosomal chloride transporter CLH-6 protects lysosome membrane integrity via cathepsin activation. *J. Cell Biol.* 222:e202210063. https://doi.org/10.1083/jcb.202210063

Zhang, S., Y. Liu, B. Zhang, J. Zhou, T. Li, Z. Liu, Y. Li, and M. Yang. 2020. Molecular insights into the human CLC-7/Ostm1 transporter. *Sci. Adv.* 6: eabb4747. https://doi.org/10.1126/sciadv.abb4747

Zhang, W., J. Bai, K. Hang, J. Xu, C. Zhou, L. Li, Z. Wang, Y. Wang, K. Wang, and D. Xue. 2022. Role of lysosomal acidification dysfunction in mesenchymal stem cell senescence. *Front. Cell Dev. Biol.* 10:817877. https://doi.org/10.3389/fcell.2022.817877

Zhou, C., Y. You, W. Shen, Y.Z. Zhu, J. Peng, H.T. Feng, Y. Wang, D. Li, W.W. Shao, C.X. Li, et al. 2016. Deficiency of sorting nexin 10 prevents bone erosion in collagen-induced mouse arthritis through promoting NFATc1 degradation. *Ann. Rheum. Dis.* 75:1211–1218. https://doi.org/10.1136/annrheumdis-2014-207134

Supplemental material

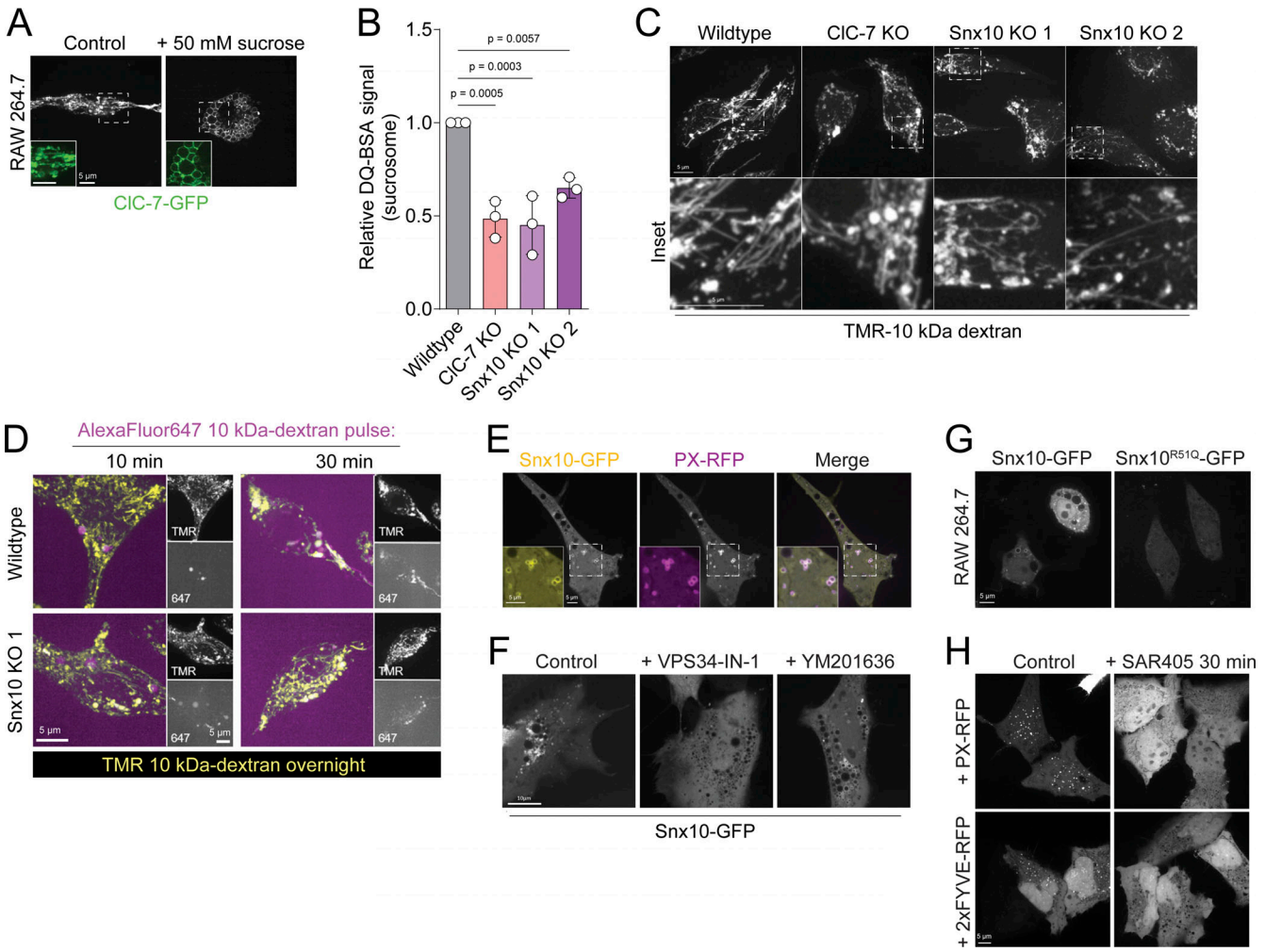

Figure S1. **Characterization of Snx10 localization and effect on endolysosomal morphodynamics. (A)** RAW 264.7 macrophages transiently transfected with ClC-7-GFP (green) for 18 h in the absence (control) or presence of 50 mM sucrose. **(B)** Relative DQ-BSA signal in sucrosomes generated in WT, ClC-7 KO, and Snx10 KO RAW 264.7 macrophages by overnight incubation with 50 mM sucrose. Cells were acutely incubated with DQ-BSA for 30 min prior to imaging. **(C)** Representative fluorescence images of lysosomes in WT, ClC-7 KO, and Snx10 KO RAW 264.7 macrophages. Lysosomes were visualized by pulsing overnight with TMR-conjugated 10 kDa dextran and chasing for 1 h prior to imaging. Lower row shows four times (4×) zoom images of regions denoted by dashed lines. **(D)** Lysosomes were visualized by pulsing overnight with TMR-conjugated 10 kDa dextran and chasing for 1 h prior to receiving a secondary pulse of AlexaFluor-647–conjugated 10 kDa dextran for 10–30 min prior to imaging, as indicated. **(E)** HeLa cells were transiently transfected with Snx10-GFP and PX-RFP 18 h prior to imaging. **(F)** HeLa cells were transiently transfected with Snx10-GFP for 18 h, then treated acutely with either DMSO only (control), 100 nM VPS34-IN-1, or 100 nM YM201636 for 1 h prior to imaging. **(G)** WT RAW 264.7 macrophages were transiently transfected with either Snx10-GFP or Snx10^{R51Q}-GFP, a variant incapable of binding PI(3)P (see Barnea-Zohar et al., 2021) for 16 h prior to imaging. **(H)** HeLa cells were transiently transfected with either PX-RFP or 2xFYVE-RFP for 18 h, then subsequently treated with either control (DMSO) or 100 nM SAR405 for 30 min prior to imaging. TMR, tetramethylrhodamine.

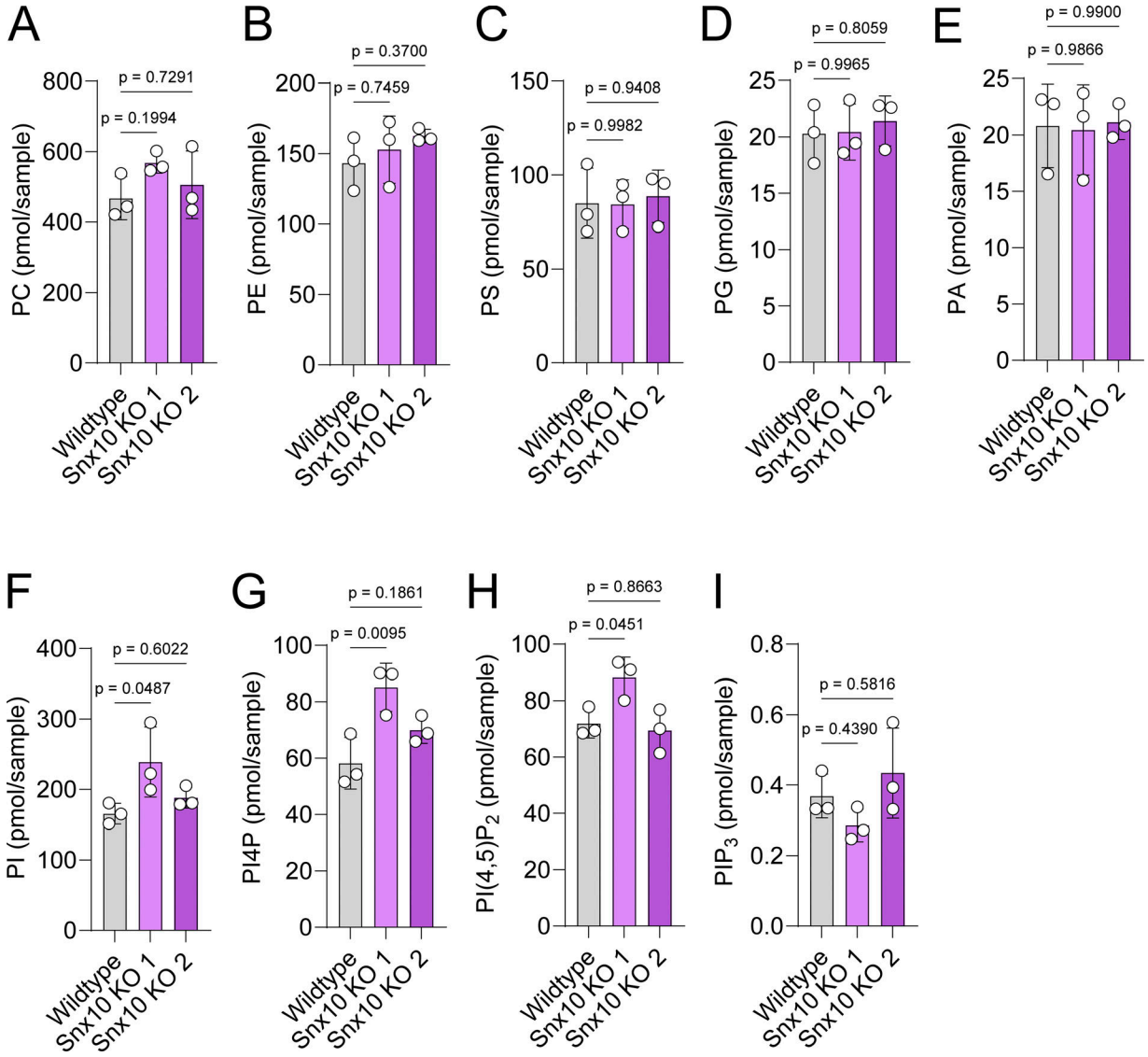

Figure S2. **Phospholipid content of WT and Snx10 KO cells. (A–H)** Levels of (A) PC, (B) PE, (C) PS, (D) PG, (E) PA, (F) PI, (G) phosphatidylinositol 4-phosphate (PI4P), (H) PI(4,5)P_2, and (I) phosphatidylinositol 3,4,5-*tris*phosphate (PIP_3) as determined by PRMC-MS. Data from three independent determinations. PRMC-MS: phosphoinositide regioisomer measurement by chiral column chromatography and mass spectrometry.

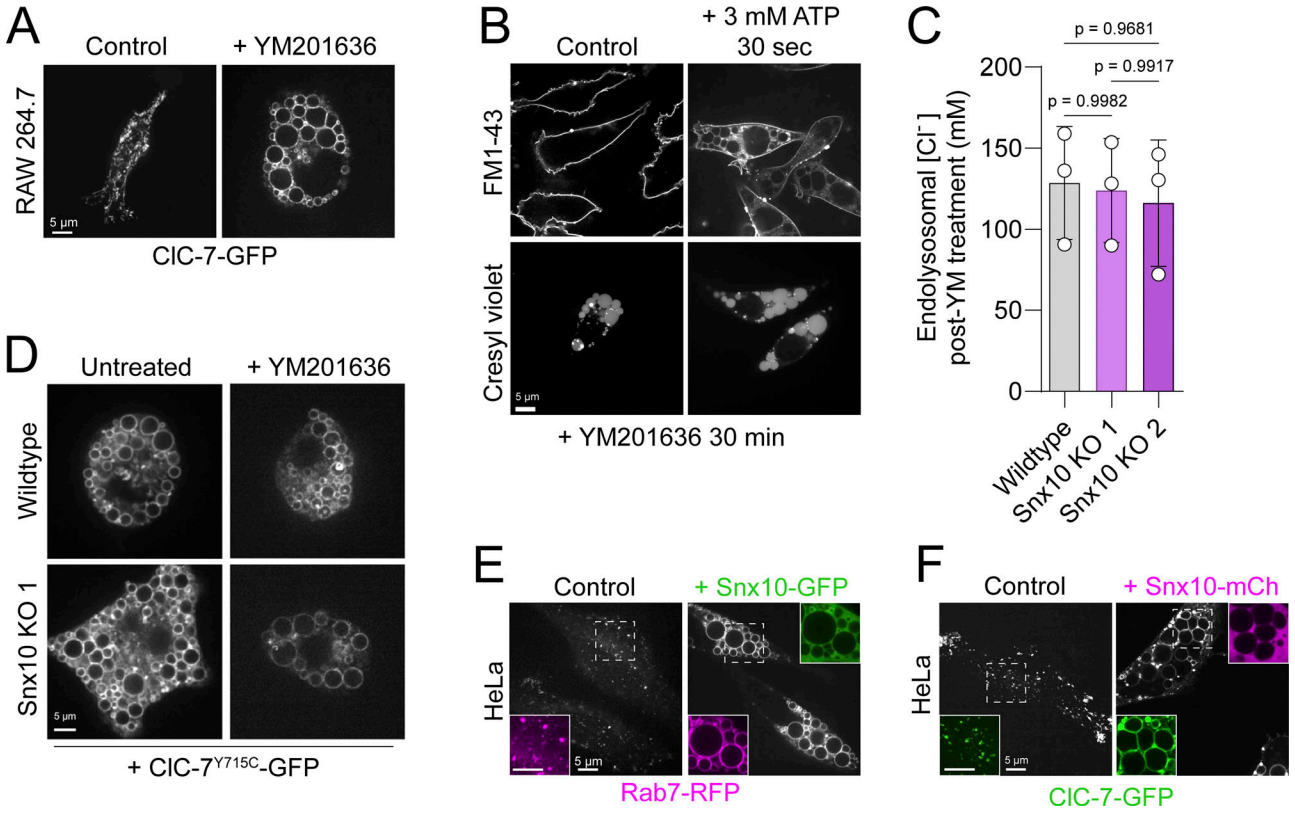

Figure S3. **Inhibition of PIKfyve maximally swells endolysosomes and restores high [Cl⁻] in Snx10 KO macrophages. (A)** WT RAW 264.7 macrophages transiently transfected with ClC-7-GFP and treated either with vehicle alone (DMSO; control) or with 100 nM YM201036 for 30 min prior to imaging. **(B)** Representative images of WT RAW 264.7 macrophages treated with 100 nM YM201636 for 30 min, then acutely treated with vehicle only (Control) or with 3 mM ATP for 30 s in Na-gluconate medium, then labeled with either FM1–43 or cresyl violet prior to imaging. **(C)** Endolysosomal [Cl⁻] was measured colorimetrically in WT and Snx10 KO RAW 264.7 macrophages as detailed in Materials and methods. **(D)** WT and Snx10 KO RAW 264.7 macrophages transiently transfected with ClC-7^{Y715C}-GFP for 12 h were either untreated or treated with YM201636 for 30 min prior to imaging. **(E)** HeLa cells were transiently transfected with Rab7-RFP (magenta). Where indicated, (right panel) the cells were also co-transfected to overexpress Snx10-GFP. **(F)** HeLa cells were transiently transfected with ClC-7-GFP with and without co-transfection (overexpression) of Snx10-mCherry. All images are representative of ≥3 similar experiments of each type.

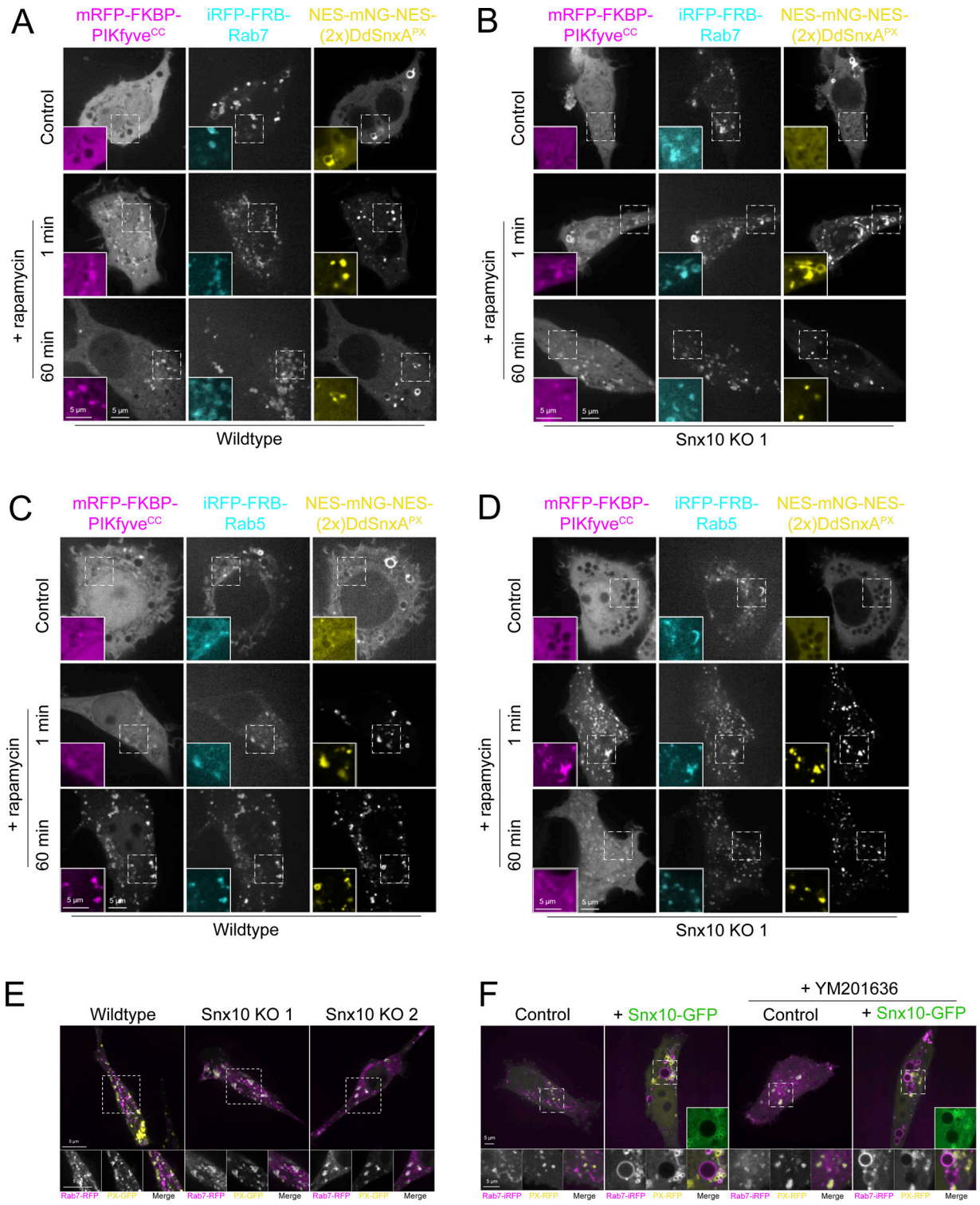

Figure S4. **Snx10 controls the levels of PI(3,5)P_2 on late endolysosomes. (A–F)** Representative images of the experiments summarized in Fig. 6, E–H; see the legend of Fig. 6 for experimental details.

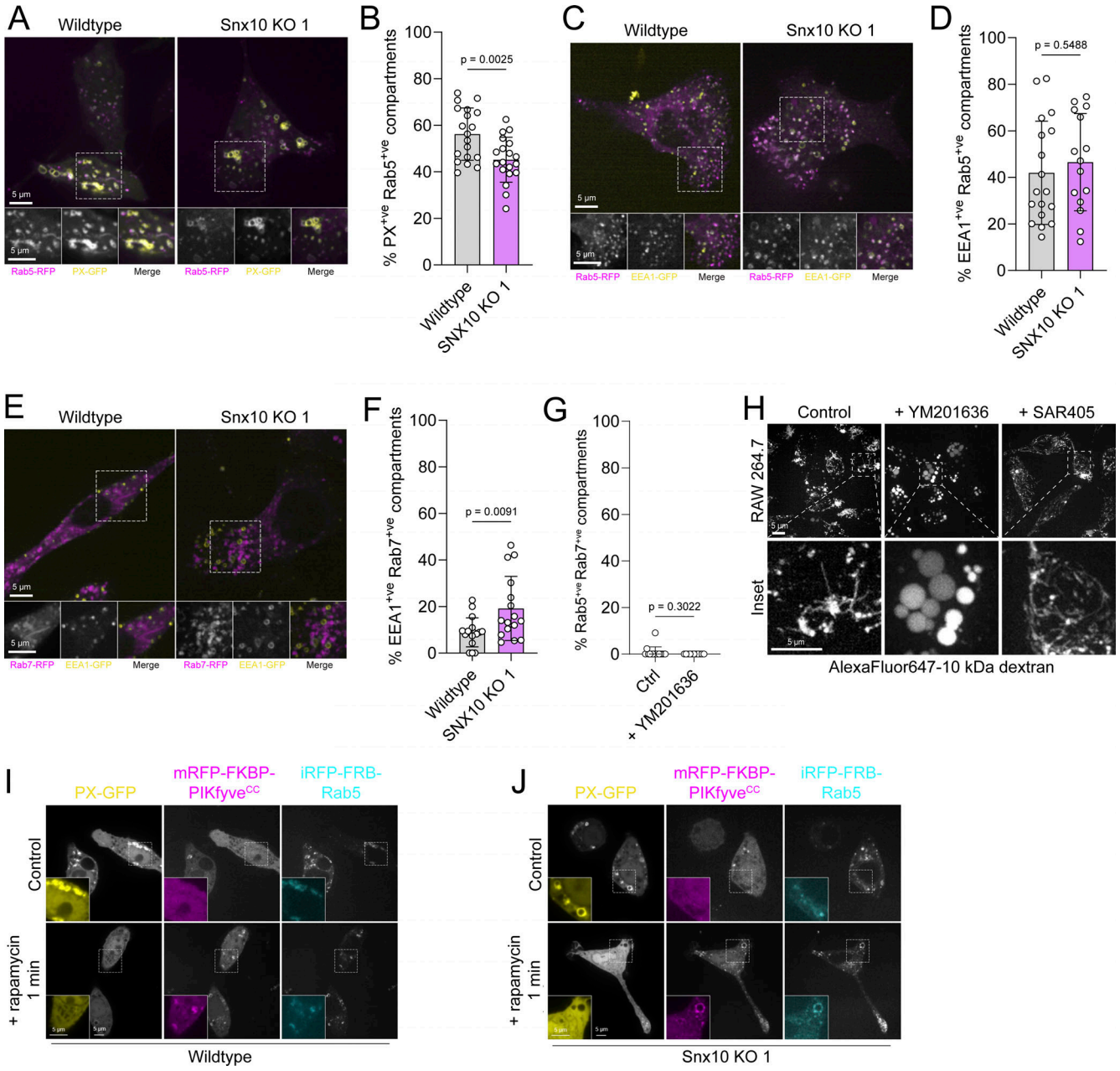

Figure S5. **Characterization of PI(3)P and its effectors on endosomes. (A)** WT and Snx10 KO RAW 264.7 macrophages were co-transfected with PX-GFP and mRFP-Rab5. The percentage of organelles found to be positive for both markers is shown in B; *n* = 3. **(C–F)** WT and Snx10 KO RAW 264.7 macrophages were co-transfected with EEA1-GFP and (C) mRFP-Rab5 or (E) mRFP-Rab7. The percentage of (C) Rab5 or (E) Rab7 compartments found to be positive for EEA1 is indicated in D and F, respectively; *n* = 3. **(G)** HeLa cells were co-transfected with mRFP-Rab5 and EGFP-Rab7 and treated with either vehicle alone (control) or with 100 nM YM201636 for 30 min prior to imaging. Shown is the percentage of Rab5-positive puncta that were also Rab7 positive. *n* = 3. **(H)** WT RAW 264.7 macrophages pulsed overnight with AlexaFluor-647–conjugated 10 kDa dextran and chased for 1 h with fresh medium were treated for 20 min with either vehicle control (left), 100 nM YM201636 (middle), or 50 nM SAR405, a selective VPS34 inhibitor (right) prior to imaging. **(I and J)** (I) WT and (J) Snx10 KO RAW 264.7 macrophages were transiently transfected with mRFP-FKBP-PIKfyve^{CC}, iRFP-FRB-Rab5, and PX-GFP 16 h prior to imaging. Representative fluorescence images of cells prior to (top 3 panels) and 1 min after the addition of 100 nM rapamycin (bottom 3 panels).

Provided online are Table S1, Table S2, Table S3, Table S4, and Table S5. Table S1 shows the plasmids. Table S2 shows the reagents. Table S3 shows the antibodies. Table S4 shows the MRM transitions for phosphoinositides. Table S5 shows the MRM transitions for PC, PE, PA, PG, and PS.